Experimental investigation on cold-formed steel stiffened lipped channel columns undergoing local-distortional interaction

Man-Tai Chen[1], Ben Young[2], André Dias Martins[3], Dinar Camotim[4], Pedro Borges Dinis[5]

Abstract
The objective of this work is to report a careful experimental investigation, planned at the University of Lisbon and carried out at The University of Hong Kong, concerning the behaviour and ultimate strength of cold-formed steel web-flange-stiffened (WFSLC) and web-stiffened (WSLC) lipped channel columns undergoing local-distortional (L-D) interaction. It involves 31 specimens (16 WFSLC+ 15 WSLC), brake-pressed from high-strength zinc-coated grades G450, G500 and G550 structural steel sheets, exhibiting critical distortional-to-local buckling load ratios ranging between 0.75 and 1.88. The column geometries were carefully selected to enable testing fixed-ended columns undergoing true L-D interaction and secondary distortional-bifurcation L-D interaction (ensuring evidence of the latter required selecting rather slender columns) – all tested specimens exhibited the expected L-D interactive failures. The specimen material properties were obtained from tensile coupon tests and their initial geometrical imperfections were measured prior to testing. The experimental results presented and discussed consist of column (i) load-displacement equilibrium paths, (ii) photos evidencing the evolution of the column deformed configurations along those paths (including the failure mode) and (iii) failure loads. Finally, the experimental failure load data obtained are compared with their estimates provided by the currently codified DSM design approaches for columns failing in L and D modes, showing their inadequacy to handle L-D interactive failures – the fresh light shed by this comparison will contribute to the timely codification, in the near future, of a DSM design procedure for columns affected by L-D interaction.

1. Introduction
It is well known that thin-walled open-section cold-formed steel (CFS) columns are highly susceptible to several instability phenomena, involving either local (L), distortional (D) or global (G) buckling, or any coupling between them, *i.e.*, L-D, L-G, D-G or L-D-G interaction – see the recent state-of-the-art report concerning CFS members affected by interactive buckling phenomena (Camotim *et al*. 2018). This investigation deals exclusively with columns affected by L-D interaction and aims at providing additional experimental failure loads associated with collapses in L-D interactive modes.

---

[1] Assistant Professor, Shanghai Jiao Tong University, <mantai.chen@sjtu.edu.cn> (formerly: Postdoctoral Researcher, The University of Hong Kong)
[2] Professor, The Hong Kong Polytechnic University, ben.young@polyu.edu.hk (formerly: Professor, The University of Hong Kong)
[3] Postdoctoral Researcher, Instituto Superior Técnico, University of Lisbon, <andrerdmartins@tecnico.ulisboa.pt>
[4] Professor, Instituto Superior Técnico, University of Lisbon, <dcamotim@civil.ist.utl.pt>
[5] Assistant Professor, Instituto Superior Técnico, University of Lisbon, <dinis@civil.ist.utl.pt>

A significant amount of work has been devoted to investigate the behavioural features inherent to this relevant coupling phenomenon in short-to-intermediate columns. Indeed, such investigations deal with (i) shell finite element analysis (*e.g.*, Martins *et al.* 2015, Dinis & Camotim 2015), (ii) Generalised Beam Theory (GBT)-based investigations used to assess the mechanics underlying this coupling phenomenon (*e.g.*, Martins *et al.* 2018), (iii) design proposals (*e.g.*, Silvestre *et al.* 2012, Martins *et al.* 2017a, Matsubara *et al.* 2019), mostly based on the Direct Strength Method (DSM) concepts (Schafer 2008, Camotim *et al.* 2016, Schafer 2019), and (iv) experimental investigations (discussed next). Although a significant number of experimental results concerning the behaviour and strength of CFS columns affected by local-distortional (L-D) interaction is available in the literature, most of them dealing with lipped channels, specimens providing clear experimental evidence of this coupling phenomenon and ensuing failure load erosion are relatively scarce – certainly much less than those collected to propose, calibrate and validate the existing local, distortional, global and local-global DSM design curves. To the authors' best knowledge, the available experimental results evidencing the occurrence of L-D interaction in fixed-ended CFS columns are due to (i) Kwon & Hancock (1992), Young & Rasmussen (1998), Kwon *et al.* (2009), Loughlan *et al.* (2012), Young *et al.* (2013), Chen *et al.* (2019) and Matsubara *et al.* (2019), for lipped channel (LC) columns, (ii) Kwon *et al.* (2005), for LC and hat-section (H) columns, (iii) Chen *et al.* (2019), for zed-section (Z) columns, (iv) Dinis *et al.* (2014) and Chen *et al.* (2019), for rack-section (R) columns, (v) Chen *et al.* (2019), for channel columns with "return lips" (RLC), (vi) Kwon & Hancock (1992), Kwon *et al.* (2009), Yap & Hancock (2011), He *et al.* (2014) and Chen *et al.* (2019), for web-stiffened lipped channel (WSLC) columns, (vii) Yang & Hancock (2004), for web/flange-stiffened lipped channel (WFSLC) columns, and (viii) Yap & Hancock (2008), for columns with complex-stiffened cross-sections, totalling 134 test results. Naturally, reliable and illuminating experimental data are essential to establish efficient DSM-based design rules to handle column L-D interactive failures, which are still lacking in the current CFS specifications worldwide. Aiming to fill this gap, Martins *et al.* (2017a) recently proposed a well-founded preliminary version of the sought DSM-based design approach. It just needs to be "fine-tuned", a task that (i) requires carefully obtained fresh experimental failure loads, namely those reported in this paper, and (ii) should pave the way for codification – the final goal of this research effort.

The main objective of this work is to present a careful experimental investigation, planned at the University of Lisbon and carried out at The University of Hong Kong, concerning the behaviour and ultimate strength of CFS WFSLC and WSLC columns undergoing L-D interaction. It comprises 31 specimens (16 WFSLC and 15 WSLC) (i) brake-pressed from high-strength zinc-coated structural steel sheets of grades G450, G500 and G550, and (ii) exhibiting distortional-to-local critical buckling load ratios ranging between 0.8 and 1.9. The column geometries selected, discussed in Section 2, were carefully chosen to enable the testing of fixed-ended columns undergoing (i) "true L-D interaction", *i.e.*, with nearly coincident critical local and distortional buckling loads, and (ii) "secondary distortional-bifurcation L-D interaction", *i.e.*, with the non-critical (distortional) buckling load visibly above the critical (local) one. Acquiring clear evidence of the latter L-D interaction required selecting rather slender columns – their measured dimensions are presented in Section 3.1. The specimen material properties were obtained from tensile coupon tests (Section 3.2) and their initial geometrical imperfections were measured prior to testing (Section 3.4). After addressing the set-up procedure, in Section 3.3, the experimental results are presented in Section 3.5 and consist of column (i) load-displacement equilibrium paths, (ii) deformed configuration evolutions along those paths, including the failure mode, and (iii) failure loads. Finally, in Section 4, the experimental failure load data obtained are compared with their estimates yielded by the currently codified DSM design curves for columns failing in pure L or D modes, providing additional clear experimental evidence that these design curves are unable to handle

adequately L-D interactive failures. Moreover, the fresh light shed by this comparison will contribute to the timely codification of an efficient (safe, accurate and reliable) DSM design procedure in the near future.

2. Column geometry selection

The success of any experimental investigation is directly linked to its planning. In the present case, the selection of the specimen geometry plays a pivotal role in achieving the objectives proposed. The aim of this test campaign is to obtain experimental failure loads of fixed-ended columns exhibiting WSLC and WFSLC cross-sections, and having distortional-to-local critical buckling load ratios ($R_{DL}=P_{crD}/P_{crL}$) varying between 0.8 and 2.0 (approximately), *i.e.*, prone to either (i) "true L-D interaction" ($0.8<R_{DL}<1.3$)[6] or (ii) "secondary distortional-bifurcation L-D interaction" ($R_{DL}>1.3$) (Martins *et al*. 2015). Note that, columns having $R_{DL}<1.3$ are prone to distortional or "secondary local-bifurcation L-D interaction" – since the latter are characterised by a negligible failure load erosion (*i.e.*, are adequately handled by the current DSM distortional design curve), they fall outside the scope of this investigation. In order to reach the sought column specimen geometries, their selection procedure should:

(i)   provide specimens characterised by $0.8<R_{DL}<2.0$ (as previously discussed);

(ii) be associated with critical global buckling loads (P_{crG}) much higher than their P_{crD} and P_{crL} counterparts (to avoid the interaction with the global buckling mode, *i.e.*, L-D-G interaction), and

(iii) identify columns prone to "secondary distortional-bifurcation L-D interaction" that are (locally) slender, since stocky columns with $R_{DL}>1.3$ are prone to local failure and exhibit no interaction.

On the other hand, the column selection procedure is "constrained" by the following limitations:

(i)   specimens with lengths not exceeding L=3000mm (testing machine limitation);

(ii) specimens without small lip and stiffeners widths (manufacturing limitation);

(iii) thickness values and steel grades of t=1.0mm (G550), t=1.2mm (G500) or t=1.5mm (G450), and

(iv) failure loads (P_{Exp}) not exceeding 220kN (load actuator capacity) – to ensure this condition, materially and geometrically non-linear shell finite element analyses (not addressed here) were conducted and showed that all the selected specimen have expected failure loads well below the above limit value (as presented in Section 3.5.2).

The column selection procedure was conducted through and "trial-and-error" approach by means of the GBT-based code GBTUL (Bebiano *et al*. 2018), mainly due to its computational efficiency and modal nature – note that, for the sake of simplicity, the round corners were neglected since they are typically lower than the wall thickness. In addition, the Young's modulus and the Poisson's ratio were considered equal to 210GPa and 0.30, respectively. Table 1 shows the output of this selection procedure and displays the obtained cross-section dimensions (D, B, b_l, t – see Fig. 1, and length L), critical (global, local and distortional) buckling loads, critical distortional half-wave number (indicated between brackets in the column P_{crD}), R_{DL} value and local (λ_L) and distortional slenderness (λ_D) – the v-shape (45º) stiffener widths b_{ws} and b_{fs} (see Fig. 1) were considered equal to 15√2mm in

---

[6] At this stage, it should be mentioned that these R_{DL} values, providing the "boundaries" between "true L-D interaction" and "secondary local or distortional-bifurcation L-D interaction", are only approximate and somewhat arbitrary – they are just intended to identify, with reasonable accuracy, the columns undergoing strong L-D interaction. These values were first proposed by the authors (Martins *et al*. 2015), in the context of lipped channel, hat-section, zed-section and rack-section columns. Subsequently, it was found that they apply also to web-stiffened (Martins *et al*. 2016) and web-flange-stiffened (Martins *et al*. 2017b) lipped channel columns, even if this information is not provided explicitly in the above references.

Table 1: Selected column specimen (i) geometries, (ii) critical local, distortional and global buckling loads, and (iii) local and distortional slenderness

Specimen	D	B	b_l	t	L	Steel	f_y	P_{crG}	P_{crL}	P_{crD}	R_{DL}	λ_L	λ_D
	(mm)	(mm)	(mm)	(mm)	(mm)	Grade	(MPa)	(kN)	(kN)	(kN)	(-)	(-)	(-)
WS-1	280	150	17	1.5	2500	G450	530	1776	86.0	71.2(2)	**0.83**	2.41	2.64
WS-2	280	150	17	1.5	2200	G450	530	2293	86.2	77.7(1)	**0.90**	2.40	2.53
WS-3	220	130	17	1.5	1700	G450	530	2181	98.4	95.5(1)	**0.97**	2.06	2.09
WS-4	220	130	17	1.5	1500	G450	530	2801	98.3	100.0(1)	**1.02**	2.06	2.05
WS-5	260	150	17	1.5	1800	G450	530	3005	84.3	81.8(1)	**0.97**	2.39	2.43
WS-6	260	150	17	1.5	1550	G450	530	4052	84.2	88.6(1)	**1.05**	2.39	2.33
WS-7	270	160	17	1.5	1500	G450	530	4928	77.8	86.9(1)	**1.12**	2.55	2.41
WS-8	270	160	17	1.5	1650	G450	530	4073	77.7	81.3(1)	**1.05**	2.55	2.49
WS-9	270	170	17	1.2	1650	G500	560	3447	36.7	53.3(1)	**1.45**	3.47	2.88
WS-10	270	170	17	1.2	1950	G500	560	2468	36.7	47.0(1)	**1.28**	3.47	3.06
WS-11	250	150	17	1.0	1750	G550	600	1973	24.8	40.7(1)	**1.64**	3.47	2.96
WS-12	250	150	17	1.0	1650	G550	600	2219	24.8	42.7(1)	**1.72**	3.80	2.89
WS-13	250	150	17	1.0	1350	G550	600	3315	24.8	50.7(1)	**2.04**	3.80	2.66
WFS-1	250	200	17	1.0	1750	G550	600	2431	63.2	51.9(1)	**0.82**	2.62	2.89
WFS-2	250	200	17	1.0	1650	G550	600	2735	63.2	56.8(1)	**0.90**	2.62	2.76
WFS-3	250	200	17	1.0	1500	G550	600	3309	63.7	66.1(1)	**1.04**	2.61	2.56
WFS-4	250	220	17	1.2	1250	G500	560	6159	113.2	108.7(1)	**0.96**	2.20	2.25
WFS-5	270	240	17	1.2	1300	G500	560	7162	102.6	101.3(1)	**0.99**	2.40	2.42
WFS-6	270	180	17	1.0	1700	G550	600	2749	53.2	56.4(1)	**1.06**	2.81	2.73
WFS-7	280	190	20	1.0	2000	G550	600	2298	51.5	54.9(1)	**1.07**	2.93	2.84
WFS-8	250	220	17	1.0	1350	G550	600	4400	65.6	76.8(1)	**1.17**	2.64	2.44
WFS-9	270	180	17	1.0	1400	G550	600	4054	53.4	76.0(1)	**1.42**	2.81	2.35
WFS-10	270	180	17	1.0	1500	G550	600	3531	53.4	68.2(1)	**1.28**	2.81	2.48
WFS-11	280	190	20	1.0	1500	G550	600	4085	51.7	82.4(1)	**1.59**	2.92	2.32
WFS-12	300	200	20	1.0	1650	G550	600	4042	47.0	71.3(1)	**1.52**	3.15	2.56
WFS-13	300	200	20	1.0	1500	G550	600	4891	46.9	80.9(1)	**1.72**	3.15	2.40

all specimens. The close observation of this table shows that (i) all the aforementioned requirements are satisfied and (ii) a total of 26 (13 WFSLC+ 13 WSLC) specimens were selected. Indeed, there are (i) 14 specimens with t=1.0mm (grade G550), labelled WS-11, 12, 13 and WFS-1, 2, 3, 6, 7, 8, 9, 10, 11, 12, 13, (ii) 4 specimens with t=1.2mm (grade G500), labelled WS-9, 10, and WFS-4, 5, and (iii) 8 specimens with t=1.5mm (grade G450), labelled WS-1, 2, 3, 4, 5, 6, 7, 8 and (iv) only one specimen with a critical distortional buckling mode exhibiting two half-waves (WS-1). For illustrative purposes, Fig. 2(a)-(c) shows the critical local (1) and distortional (2) buckling mode shapes of columns WS-1, WS-13 and WFS-5, respectively – note that local buckling is triggered by the web and flanges, respectively in all WSLC and WFSLC columns.
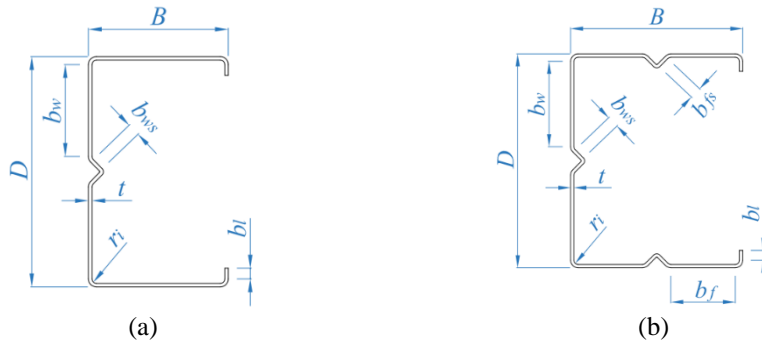

Figure 1: Cross-section shapes and dimensions of (a) web-stiffened, and (b) web-flange-stiffened lipped channels.
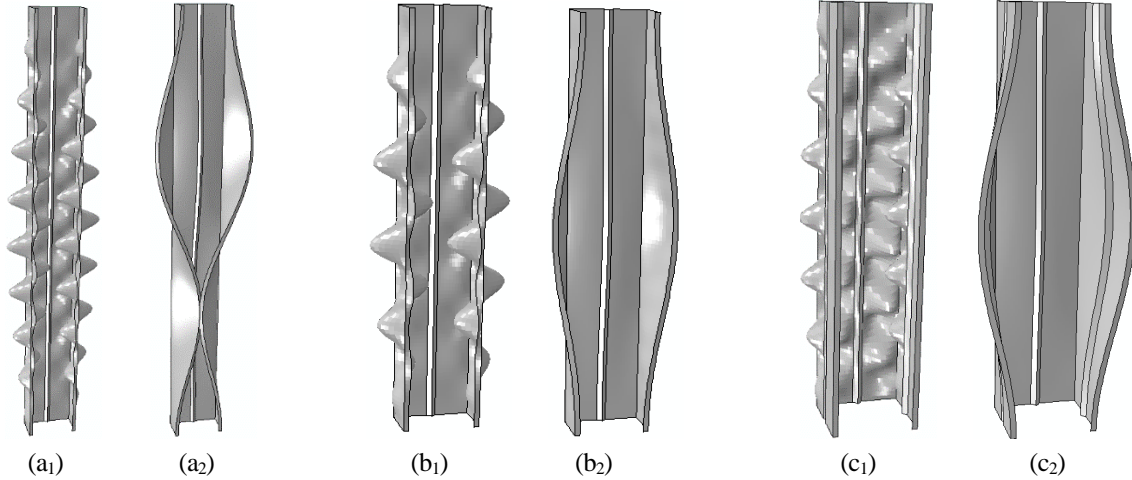
Figure 2: Critical ($_1$) local and ($_2$) distortional buckling mode shapes of columns (a) WS-1, (b) WS-13 and (c) WFS-5.

3. Experimental investigation

3.1 Test specimens

The CFS test specimens were brake-pressed from high strength zinc-coated grades G450, G500 and G550 structural steel sheets having nominal yield stresses of 450, 500 and 550MPa, respectively. The ends of the column specimens were welded to 16mm thick steel end plates, to ensure full contact between the specimen end cross-sections and bearing plates. The base metal thickness (t^*) was measured by removing the zinc coating by acid-etching. The thickness of the zinc coating, measured on one side of the cross-section, was (i) 23.5/21.5/26.0μm for wall thickness 1.0/1.2/1.5mm (WSLC specimens) and (ii) 30.5/22.5μm for wall thickness 1.0/1.2mm (WFSLC specimens). The measured cross-section dimensions, cross-section area (A) and length (L) for each specimen are shown in Table 2 (definitions/nomenclature given in Fig. 1). Note that, in order to assess the reliability of the test procedure, five pairs of specimens with nearly coincident dimensions were considered, namely WS-5+5R, WS-6+6R, WFS-5+5R, WFS-6+6R and WFS-9+9R (see Table 2).

3.2 Material properties

Tensile coupon tests were conducted to determine the material properties of the CFS WSLC and WFSLC column specimens. The coupons were extracted, in the longitudinal direction, from the central part of the unstiffened portions of the webs of specimens WFS-4, WFS-8, WS-4, WS-9 and WS-13, covering all the distinct wall thickness and cross-section shape considered in this investigation. The column specimens with the same nominal wall thickness and steel grade were fabricated from the same batch of steel. For instance, the material properties obtained from specimen WFS-4 ($t \cong 1.20$mm) were deemed similar to those of the other specimens sharing the same wall thickness and steel grade, *i.e.*, specimens WFS-5 and WFS-5R (see Table 1) – the same "extrapolation" was made for all the other specimens.

The coupon dimensions were determined according to the American standard ASTM-E8M (2016) (tensile testing of metals) using 12.5mm wide coupons of gauge length 50mm. An MTS displacement-controlled testing machine using friction grips was used to conduct the coupon tests. In addition, the coupons were tested according to the recommendations of Huang & Young (2014) for cold-formed carbon steel. A calibrated extensometer of 50 mm gauge length was used to measure the coupon specimen longitudinal strains. A data acquisition system was used to record the load and the strain readings at regular intervals during the tests. The tests were paused for 100 seconds near the 0.2% proof stress and the ultimate tensile strength, to allow for the stress relaxation associated with plastic straining

Table 2: Measured cross-section dimensions, lengths and cross-section area of the tested specimens (WSLC and WFSLC).

Specimen	D (mm)	B (mm)	b_l (mm)	b_f (mm)	b_w (mm)	b_{fs} (mm)	b_{ws} (mm)	t (mm)	t^* (mm)	r_i (mm)	L (mm)	A (mm²)
WS-1	279.6	150.5	15.7	-	122.0	-	18.6	1.565	1.513	0.97	2501	969.9
WS-2	278.7	151.1	16.1	-	121.7	-	19.2	1.567	1.515	0.72	2201	973.2
WS-3	220.6	129.8	15.5	-	92.2	-	18.2	1.565	1.513	0.59	1701	807.1
WS-4	222.3	129.6	16.0	-	93.8	-	18.4	1.574	1.522	0.96	1502	821.3
WS-5	261.9	150.3	16.4	-	113.3	-	18.5	1.564	1.512	0.72	1803	941.5
WS-5R	262.7	149.9	16.3	-	113.2	-	18.7	1.572	1.520	0.84	1801	946.1
WS-6	258.8	150.6	16.3	-	111.4	-	18.8	1.565	1.513	0.72	1552	937.5
WS-6R	259.5	149.8	15.6	-	112.3	-	17.6	1.560	1.508	0.60	1554	927.4
WS-7	269.1	160.3	16.0	-	116.8	-	18.3	1.553	1.501	0.72	1500	974.8
WS-8	269.0	160.4	15.7	-	117.3	-	18.2	1.563	1.511	0.72	1651	981.8
WS-9	274.5	170.4	16.7	-	120.4	-	18.5	1.258	1.215	0.87	1653	826.9
WS-10	272.7	171.6	16.4	-	120.2	-	18.4	1.262	1.219	0.74	1955	830.4
WS-11	252.1	151.2	16.5	-	109.3	-	19.2	1.060	1.013	0.97	1753	634.0
WS-12	253.3	151.6	16.3	-	109.1	-	19.3	1.058	1.011	0.85	1652	632.5
WS-13	255.5	150.9	15.8	-	109.8	-	18.7	1.059	1.012	0.85	1350	630.5
WFS-1	252.4	202.2	15.9	86.7	108.5	19.4	19.0	1.052	0.991	0.72	1752	755.9
WFS-2	252.5	201.5	15.8	83.8	108.6	19.3	19.8	1.064	1.003	0.97	1652	770.5
WFS-3	252.2	201.6	15.9	83.5	108.2	19.3	18.9	1.063	1.002	0.72	1503	762.3
WFS-4	250.1	220.5	15.8	93.7	107.7	18.8	18.4	1.254	1.209	1.00	1254	951.9
WFS-5	271.4	241.2	15.0	103.2	117.2	18.6	18.6	1.263	1.218	0.62	1299	1020.8
WFS-5R	273.8	240.2	15.0	103.3	119.0	18.6	18.1	1.265	1.220	0.62	1299	1026.6
WFS-6	270.6	182.6	16.2	73.4	117.3	18.6	18.8	1.067	1.006	0.72	1702	738.5
WFS-6R	273.3	181.4	15.8	73.7	119.2	19.6	19.4	1.070	1.009	0.72	1703	750.8
WFS-7	283.8	193.2	17.2	78.0	123.7	18.6	18.5	1.055	0.994	0.72	2005	764.2
WFS-8	252.5	222.0	15.5	94.2	109.4	19.1	16.3	1.059	0.998	0.72	1355	799.6
WFS-9	273.0	182.7	17.7	73.4	119.1	19.2	18.4	1.055	0.994	0.72	1398	738.9
WFS-9R	271.5	182.1	16.4	73.6	118.8	19.5	19.8	1.071	1.010	0.84	1401	753.6
WFS-10	270.8	182.6	15.6	74.8	117.2	19.5	19.9	1.059	0.998	0.72	1504	743.5
WFS-11	282.6	191.6	17.5	78.4	122.8	19.0	20.4	1.061	1.000	0.72	1501	774.9
WFS-12	300.5	202.0	16.9	82.9	128.4	19.9	20.6	1.060	0.999	0.72	1654	818.2
WFS-13	302.6	201.6	16.7	83.0	134.0	18.1	19.2	1.069	1.008	0.72	1502	816.0

and to obtain the static stress-strain relationship. The nominal and measured material properties obtained from the coupon tests are summarised in Table 3 and include the measured values of (i) Young's modulus (E), (ii) static 0.2% proof stress ($\sigma_{0.2}$), (iii) static tensile strength (σ_u) and corresponding strain (ε_u), and (iv) elongation after rupture (ε_f) – note that, the various values obtained for the Young's modulus are very similar. The constitutive laws obtained for all the coupons analysed are very similar – for illustrative purposes, Fig. 3 shows the stress-strain (test and static) curves obtained from one coupon test analysed (specimens WFS-4 and WS-13). Naturally, the numerical analyses intended to simulate these tests must employ the appropriate true stress-strain curves, obtained from the curves displayed in Figs. 3(a)-(b).

Table 3: Nominal and measured material properties of CFS WSLC and WFSLC specimens.

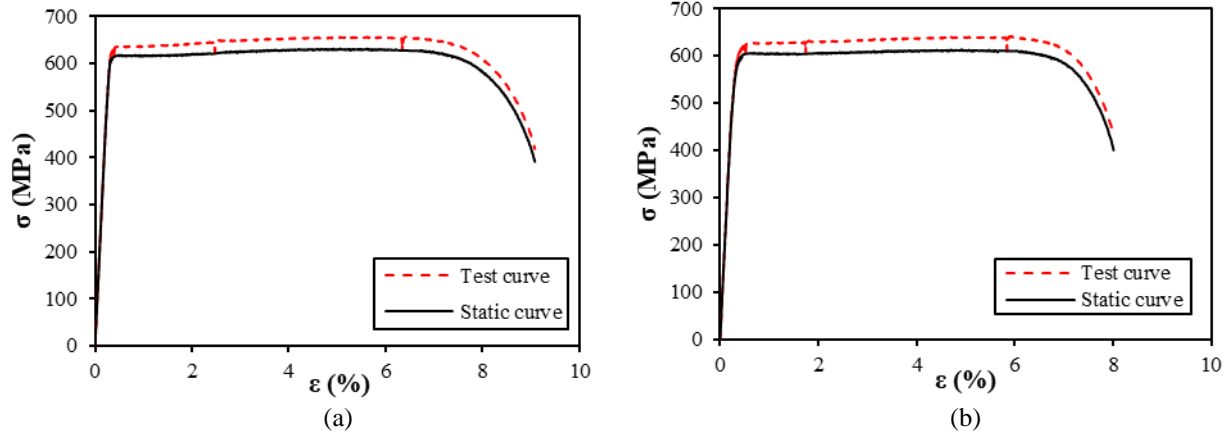| Test Series	Nominal		Measured				
	t (mm)	$\sigma_{0.2}$ (MPa)	E (GPa)	$\sigma_{0.2}$ (MPa)	σ_u (MPa)	ε_u (%)	ε_f (%)
WFS-4	1.2	500	215.2	617.2	631.4	5.1	9.1
WFS-8	1.0	550	215.6	601.7	615.4	5.0	8.3
WS-4	1.5	450	212.6	488.2	507.6	6.0	11.9
WS-9	1.2	500	214.1	612.2	627.6	5.0	8.1
WS-13	1.0	550	216.7	602.7	613.8	4.9	8.0

Figure 3: Tensile coupon tests: illustrative stress-strain curves concerning specimens (a) WFSLC-4 and (b) WSLC-13.

3.3 Test set-up and procedure

A schematic representation of the test rig and set-up employed in this investigation is shown in Fig. 4. It consists of a vertical testing frame conceived to conduct displacement-controlled tests, an essential feature in assessing geometrically non-linear behaviours involving the need to obtain a structural response after the peak load has been reached. A servo-controlled hydraulic testing machine was employed to apply a compressive axial force to the column specimens (see the top of Fig. 4), which can go up to 220kN. In addition, two thick steel plates were welded to the specimen end cross-sections (see the top and bottom of Fig. 4). The specimen top end plate was bolted to the rigid flat bearing plate, which was restrained against bending rotations about the minor and major axes, twist rotations and warping. On the other hand, a special bearing device was used at the bottom end support. Initially, this special bearing was free to rotate in any direction, since it contains a spherical hinge. Then, the actuator ram was moved slowly until the specimen bottom end plate was in full contact with the special bearing, following the imposition of a small initial load (approximately 2kN). This procedure eliminated any possible gaps between the special bearing and the specimen bottom end plate. Then, the bottom end plate was bolted to the special bearing, which was subsequently restrained against bending rotations (minor and major-axis) and twisting, by means of vertical and horizontal bolts, respectively – these bolts locked the bearing in position after full contact was achieved. Thus, the use of this special bearing makes it possible to materialise a fixed-ended support, as it restrains the end-section minor and major-axis bending rotations, twist rotations and warping.

Displacement control was used to drive the hydraulic actuator at a constant speed of 0.2mm/min for all column specimens. Moreover, in order to measure relevant displacements along the procedure, several transducers (Linear Variable Displacement Transducers – LVDTs) were installed along the specimen length – Figs. 5 and 6 show the transducer arrangement. Regardless of the cross-section shape, three longitudinal displacement transducers (A1 to A3 in Fig. 6) were installed to measure the column axial shortening. In addition, eleven (WSLC) or twelve (WFSLC) horizontal transducers were installed to measure the deformations of the mid-height cross-section – note that the horizontal transducers near the corners were located 15mm away from those same corners (*e.g.*, web-flange corners). In addition, in both specimens (see Figs. 6(a)-(b)), (i) three transducers were placed in each stiffened or flat flange (T1 to T3 and T9 to T11), to capture the corresponding in-plane distortional displacements, (ii) four transducers were placed in the stiffened web (T4, T5, T7 and T8), to capture its in-plane distortional (T4, T7 and T8) and local (T4, T5 and T7) displacements. Note also that

7

either one (T6 – WFSLC specimens) or two (T6 and T12 – WSLC specimens) additional transducers were placed 130mm away from the specimens mid-height (see Figs. 6(a)-(b)), in order to detect the cases in which the maximum displacements did not occur at the specimen mid-height − 130mm is close to the width of the flat web portions (b_w). It should be mentioned that, rigorously speaking, the horizontal transducers do not measure exclusively local and/or distortional displacements, since significant minor-axis flexure emerges as loading progresses. It is due to the effective centroid shift effects caused by the substantial cross-section stress redistribution occurring at advanced loading stages (*e.g.*, Young & Rasmussen 1999), a phenomenon that was recently quantified by means of GBT-based post-buckling analysis in (Martins *et al.* 2018) − in this case, the stress redistribution stems mainly from the distortional deformations. Lastly, it is worth noting that the characterisation of the load-displacement equilibrium paths was achieved through a data acquisition system that recorded the applied load and the readings of the displacement transducers at regular intervals during the tests.
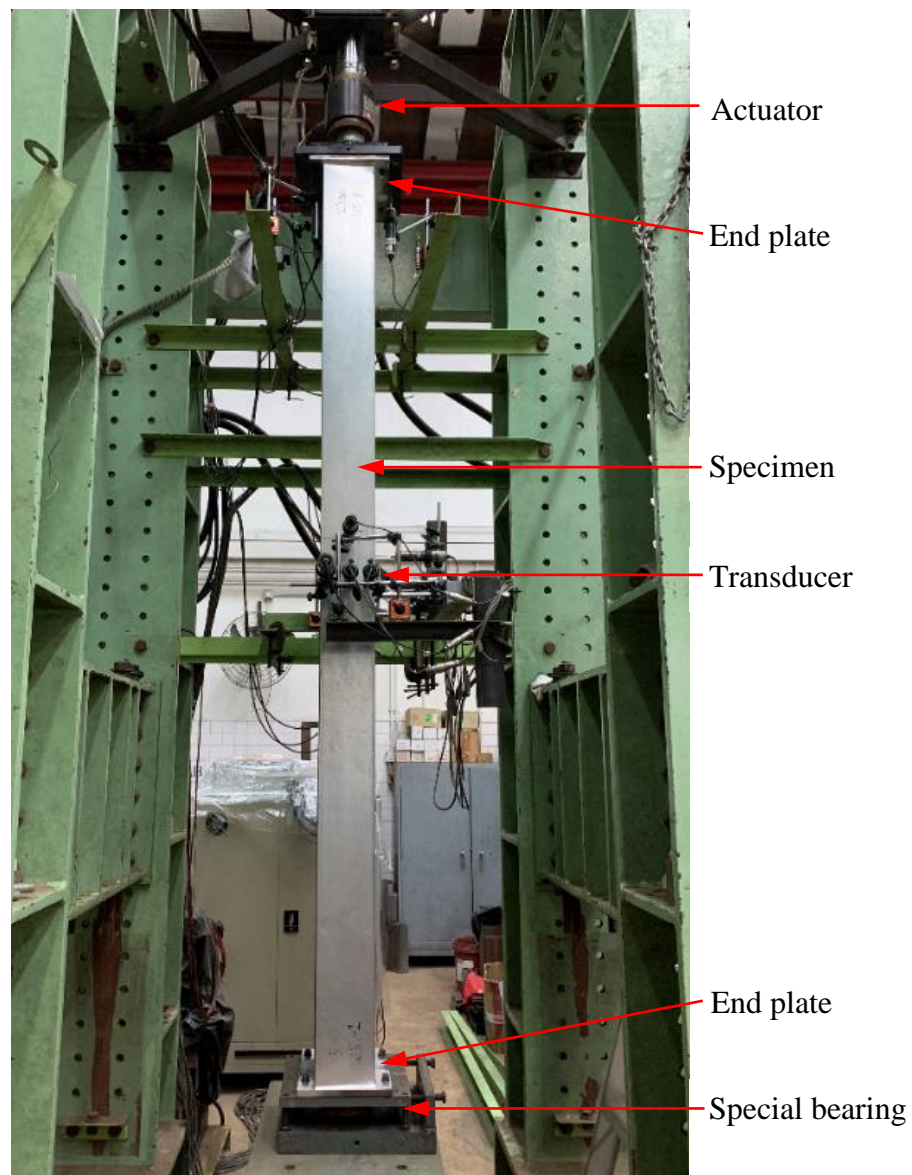

Figure 4: Fixed-ended column test rig and set-up.

Figure 5: Transducer arrangement at the mid-height cross-section of the (a) WFSLC and (b) WSLC specimens.
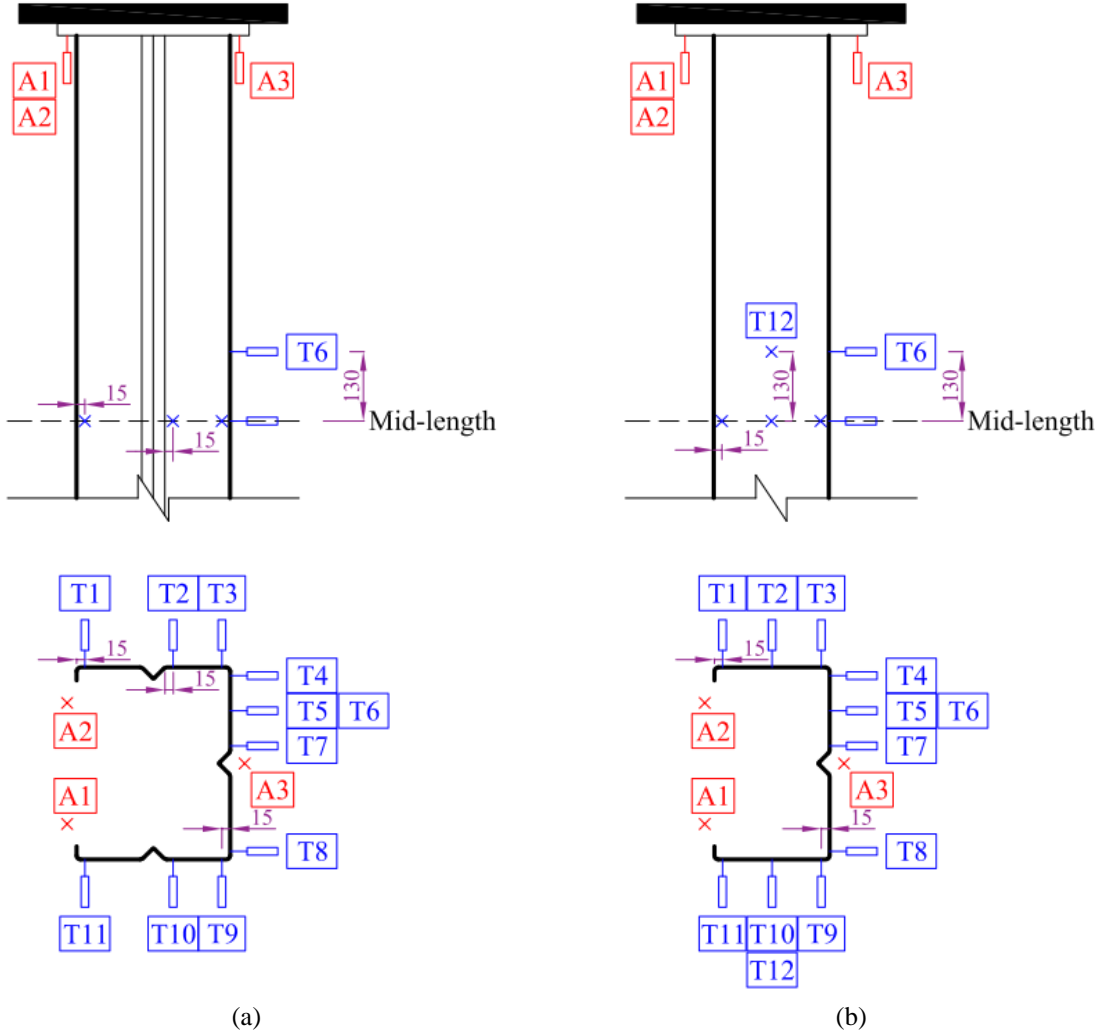

(a)   (b)

Figure 6: Location of the transducers at top and mid-height cross-sections (a) WFSLC and (b) WSLC specimens.

3.4 Initial geometrical imperfections

In order conduct future numerical simulations, initial geometrical imperfections were measured prior to testing, namely distortional and global (minor-axis flexure displacements and torsional rotations). The initial imperfection distortional component (δ_D – see Fig. 7(a)) was obtained as half the difference between the readings concerning (i) the web width D and (ii) the distance between the two flange-lip corners D_2 ($\delta_D=(D_2-D)/2$) – this imperfection component was obtained on the basis of readings provided by a theodolite at three locations: specimen top, bottom and mid-height cross-sections. The δ_D values obtained are given in Table 4, where the positive sign indicates "outward" (distortional) flange-lip motions. The minor-axis flexural (δ_F) and torsional (δ_T) initial geometrical imperfections were based on the readings indicated in Figs. 7(b)+(c), always measured at the specimen mid-height cross-section web-flange corners. These initial imperfection components are also given in Table 4, "adequately" normalised, where positive δ_F/L and $2\delta_T/D$ values indicate, respectively, (i) minor-axis bending curvatures towards the web, and (ii) clockwise torsional rotations. It is also worth mentioning that (i) only discrete displacements were measured (mainly at mid-height), which means that no initial geometrical longitudinal profiles are available, and that (ii) these specimens are rather slender (see/recall Section 2), which means that their failure loads are not significantly affected by the initial geometrical amplitude and/or shape – see Martins *et al.* (2017a).

Table 4: Measured initial geometrical imperfections for all the specimens tested: distortional and minor-axis flexure displacements, and torsional rotations (see nomenclature in Fig. 7)

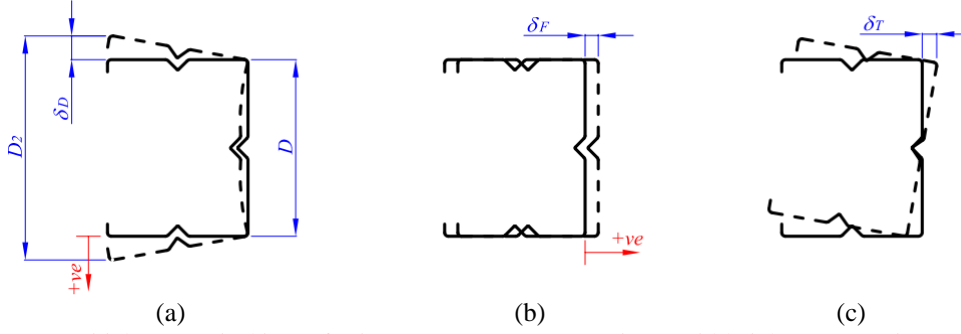| Specimen	Distortional imperfection (mm), $\delta_D = (D_2 - D)/2$			Flexural imperfection	Torsional imperfection
	Top end	Mid-height	Bottom end	δ_F /L	$2\delta_T /D$
WFS-1	7.00	12.50	2.25	-1/27375	1/181
WFS-2	6.50	12.25	7.50	1/51625	1/209
WFS-3	4.25	11.50	6.75	1/5917	1/496
WFS-4	-1.00	5.50	0.00	-1/3956	1/658
WFS-5	3.50	14.75	5.00	1/10228	1/1069
WFS-5R	0.00	8.50	1.50	0	1/269
WFS-6	7.75	11.50	4.50	1/13402	1/355
WFS-6R	8.00	13.50	6.00	0	1/359
WFS-7	0.00	2.00	4.75	-1/31328	1/172
WFS-8	2.50	10.50	3.25	1/105	1/10
WFS-9	5.66	12.30	7.44	0	1/269
WFS-9R	-0.21	3.93	-0.48	1/4420	1/428
WFS-10	7.50	10.25	5.00	1/7874	1/305
WFS-11	6.75	10.50	4.25	1/5909	1/556
WFS-12	0.25	2.75	0.75	1/6512	0
WFS-13	-2.00	4.75	1.00	-1/23841	1/217
WS-1	10.00	7.50	13.25	1/2624	1/732
WS-2	2.75	-4.50	-2.50	1/2476	1/1097
WS-3	3.25	1.75	1.25	1/2232	0
WS-4	2.00	2.00	4.00	1/2626	1/351
WS-5	4.50	2.50	5.75	1/5166	1/317
WS-5R	4.50	4.00	8.25	1/2026	1/517
WS-6	3.75	1.25	2.50	1/2037	1/509
WS-6R	-1.75	-4.50	-4.00	1/3059	0
WS-7	-0.25	-2.50	-0.50	1/2953	1/530
WS-8	-0.75	-1.25	1.75	1/8644	1/192
WS-9	-2.25	-4.50	-2.75	1/8654	1/722
WS-10	5.50	-1.25	-1.50	1/2566	1/268
WS-11	1.75	-0.75	4.00	1/1454	1/663
WS-12	4.50	0.25	0.75	1/2888	1/285
WS-13	-0.50	-1.25	4.00	1/2126	1/251

Figure 7: Initial geometrical imperfection measurements at specimen mid-height cross-section: (a) distortional displacements, (b) minor-axis flexure displacements, and (c) torsional rotation.

3.5 Test results

The experimental results obtained from this test campaign, presented and discussed in the two next sub-sections, consist of (i) load-displacement equilibrium paths and photos showing deformed configurations along those paths, including the failure mode (Section 3.5.1), and (ii) failure loads (Section 3.5.2). Before these results are addressed, Figs. 8(a)-(o) (WSLC) and Figs. 9(a)-(p) (WFSLC) display the failure modes, *i.e.*, the deformed configurations at the onset of collapse, of all the 31 specimens tested. These photos provide clear evidence of local and (mostly) distortional deformations taking place along the column, which confirms that all these specimens are affected by L-D interaction (as intended). Moreover, since most of the specimens tested exhibited similar structural responses, only a representative fraction of the results obtained for the 31 columns are presented and discussed in this manuscript.

3.5.1 Deformed configurations and equilibrium paths

3.5.1.1 True L-D interaction

This sub-section presents and discusses the structural response of four column specimens with close critical local and distortional buckling loads, namely specimens WS-1, WS-5, WFS-6 and WFS-9. Figs. 10 (WS-5), 11 (WFS-6) and 12 (WFS-9) show several views of column deformed configurations (i) along the equilibrium path ascending branch (before collapse – Figs. 10(a)-12(a)), (ii) at the onset of collapse (Figs. 10(b)-12(b)) and (iii) along the equilibrium path descending branch (after collapse – Figs. 10(c)-11(c)) or after removing the applied load (Fig. 12(c)). Fig. 13, concerning column WS-1, shows the deformed configurations prior to collapse (Fig. 13(a)) and at the onset of collapse (Fig. 13(b)). Moreover, Fig. 14 shows recorded equilibrium paths, concerning the aforementioned columns, displaying the applied load P, measured by the hydraulic actuator load cell, versus (i) the column axial shortening (average of the measurements by transducers A1, A2 and A3 – Figs. 14(a_1)-(a_4)), and the mid-height (ii) flange-lip vertical displacements (measured by transducer T1), (iii) web-top flange horizontal displacements (measured by transducer T4) and (iv) mid-top web horizontal displacements (measured by transducer T5). The observation of these results leads to the following comments:

(i)   First of all, pronounced local and distortional deformations occur in the columns prior to collapse, as shown in Figs. 10-13(a_1)-(a_4), thus attesting that these columns experience "true L-D interaction". Moreover, the columns selected (recall Section 2) were designed to exhibit high local and distortional slenderness values, which allows for the development of such pronounced deformations, which become even more visible at the onset of collapse (see Figs. 10-13(b_1)-(b_4)).

(ii) All column failure modes exhibit one or two distortional half-waves – same as the critical distortional half-wave number (recall Section 2). Except column WS-1, which exhibited two distortional half-waves, all the columns exhibit one distortional half-wave involving either "inward" or "outward"
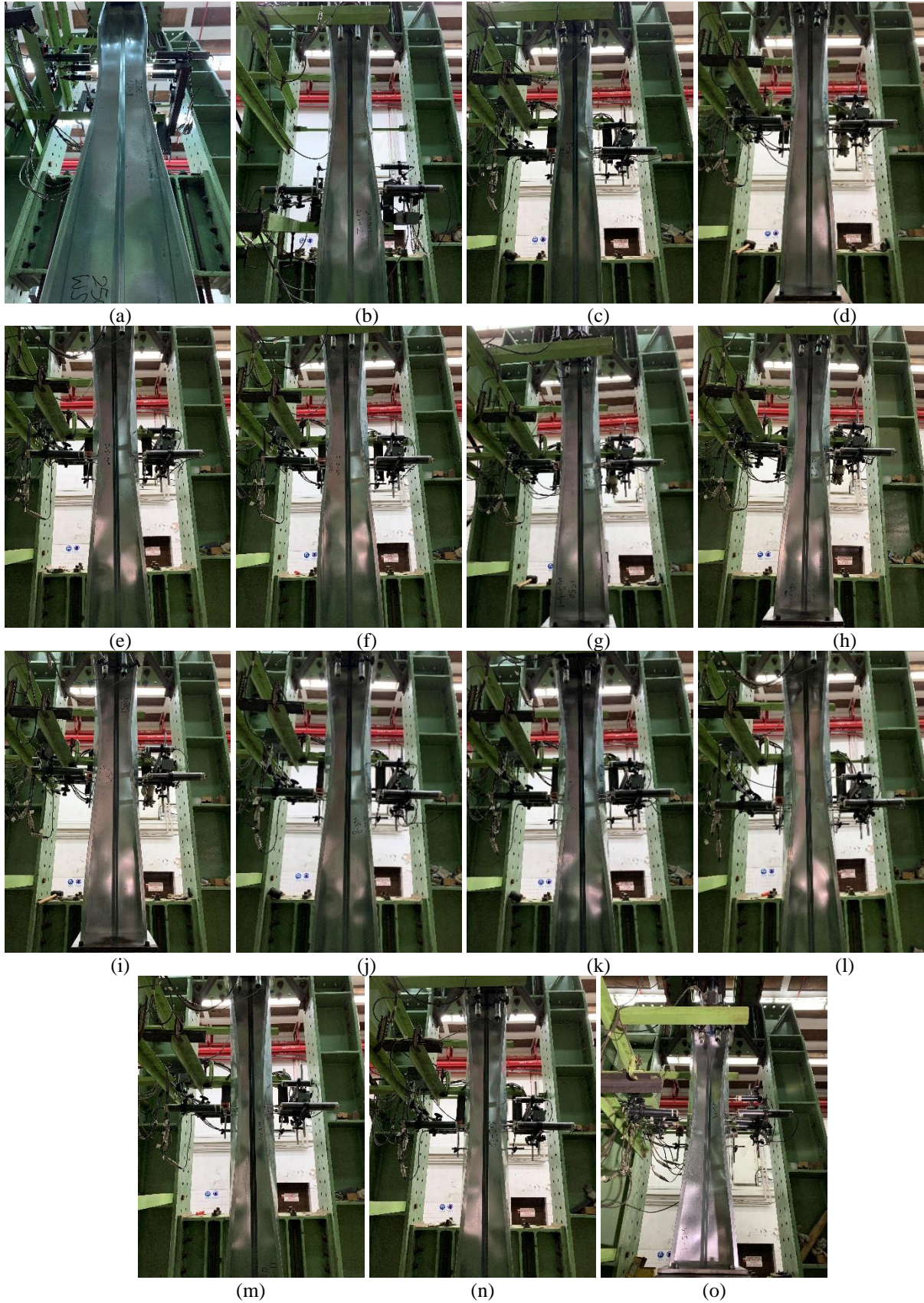
11

Figure 8: L-D interactive failure modes of WSLC specimens (a)-(o) 1, 2, 3, 4, 5, 5R, 6, 6R, 7, 8, 9, 10, 11, 12 and 13.
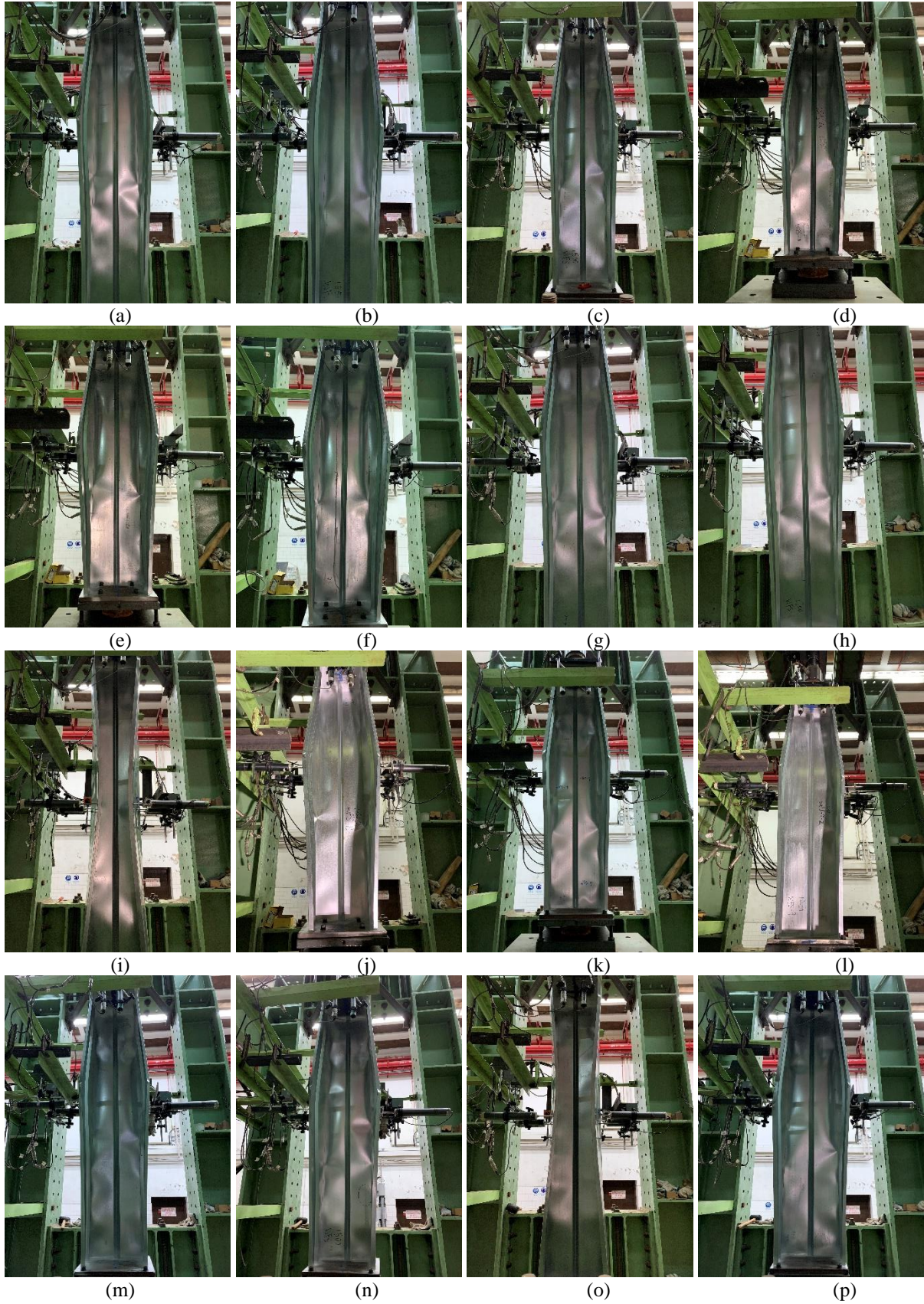
Figure 9: L-D interactive failure modes of WFSLC specimens (a)-(p) 1, 2, 3, 4, 5, 5R, 6, 6R, 7, 8, 9, 9R, 10, 11, 12 and 13.
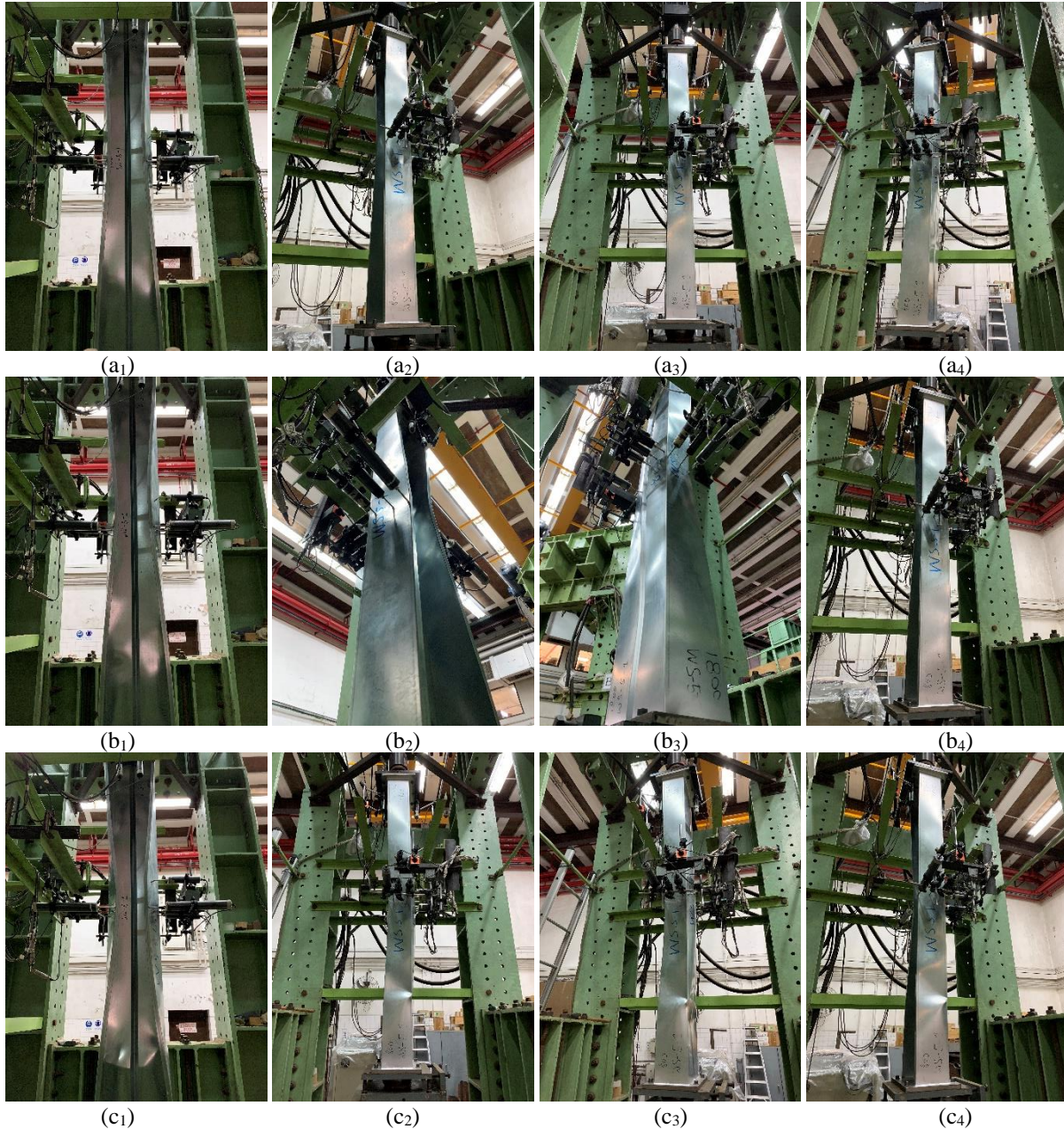
Figure 10: WSLC-5 column deformed configurations (a) prior to collapse (ascending equilibrium path), (b) at the onset of collapse (failure mode) and (c) after collapse (descending equilibrium path).

flange-lip motions. In fact, all WSLC columns (except the WS-1 one) exhibited "inward" flange-lip motions (see Fig. 8), which is in agreement with the findings reported in (Martins *et al.* 2016), where most initially imperfect columns tend to exhibit "inward" motions at fairly advanced post-buckling stages – note that, depending on the initial geometrical imperfection pattern, these columns may also exhibit "outward" flange-lip motions. On the other hand, all WFSLC columns exhibited one distortional half-wave, in most cases involving "outward" flange-lip motions, unlike their WSLC counterparts and now in close agreement with the findings reported in (Martins *et al.* 2017b). Indeed, Fig. 9 shows that 14 (out of 16) columns exhibited "outward" (distortional) flange-lip motions. As far as the local deformations are concerned, no relation can be
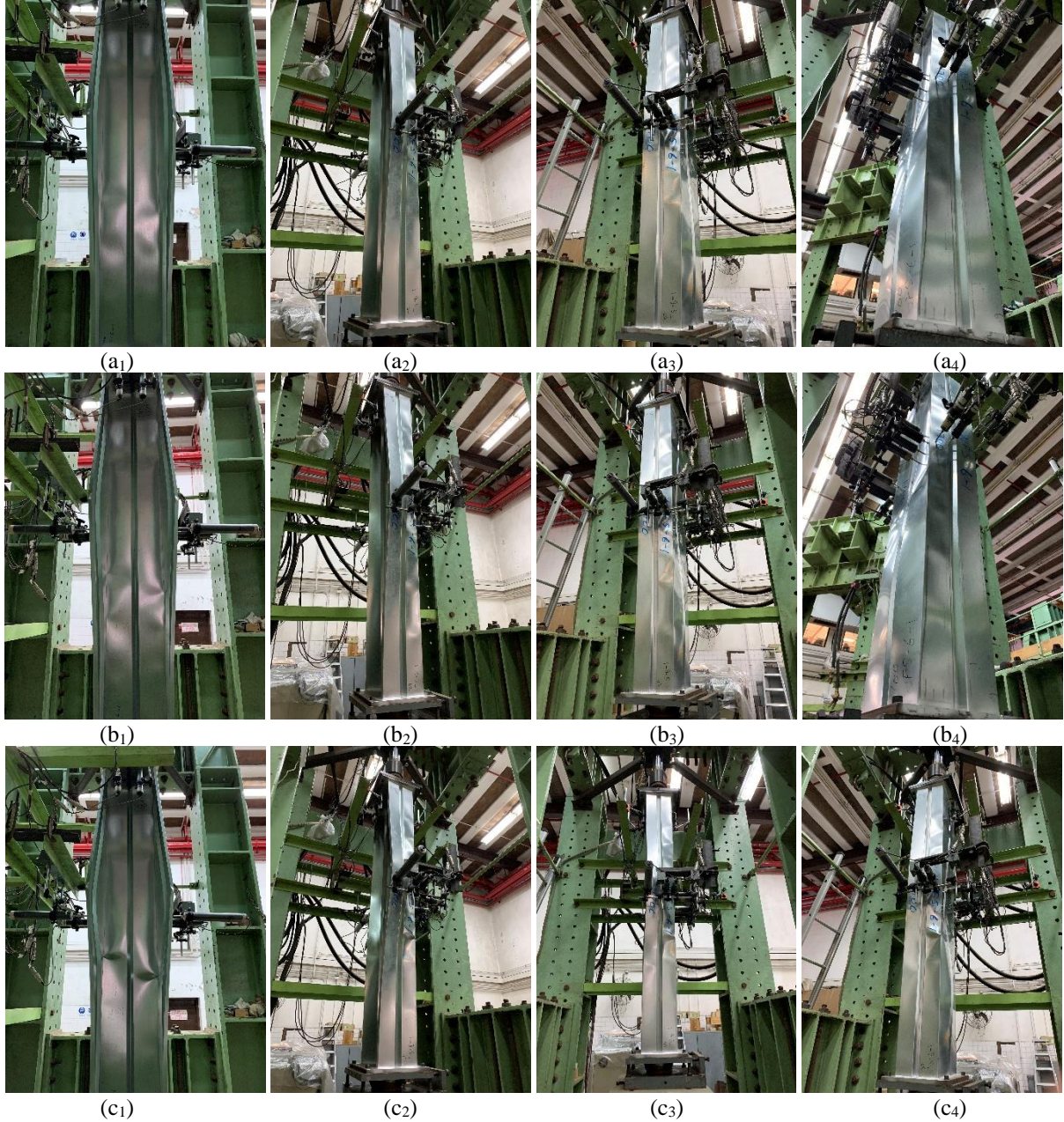
Figure 11: WFSLC-6 column deformed configurations (a) prior to collapse (equilibrium path ascending branch), (b) at the onset of collapse (failure mode) and (c) after the collapse (equilibrium path descending branch).

established with the critical local buckling modes as was reported in (Martins *et al.* 2018) – since the distortional deformations are always highly dominant, no information about the number of local half-waves can be obtained from the measurement of (any) displacement longitudinal profile.

(iii) The plastic hinges appear either near the end regions or at mid-span, and are also in close agreement with the numerical results reported in (Martins *et al.* 2016, 2017). The main difference between the experimental and numerical features occurs in the columns with plastic hinges near the end regions: two plastic hinges, equally distant from each end, are obtained numerically, while only one is observed experimentally – this is most likely due to the non-symmetry exhibited by the initial geometrical imperfections, unlike the critical-mode imperfections involved in the numerical simulations.
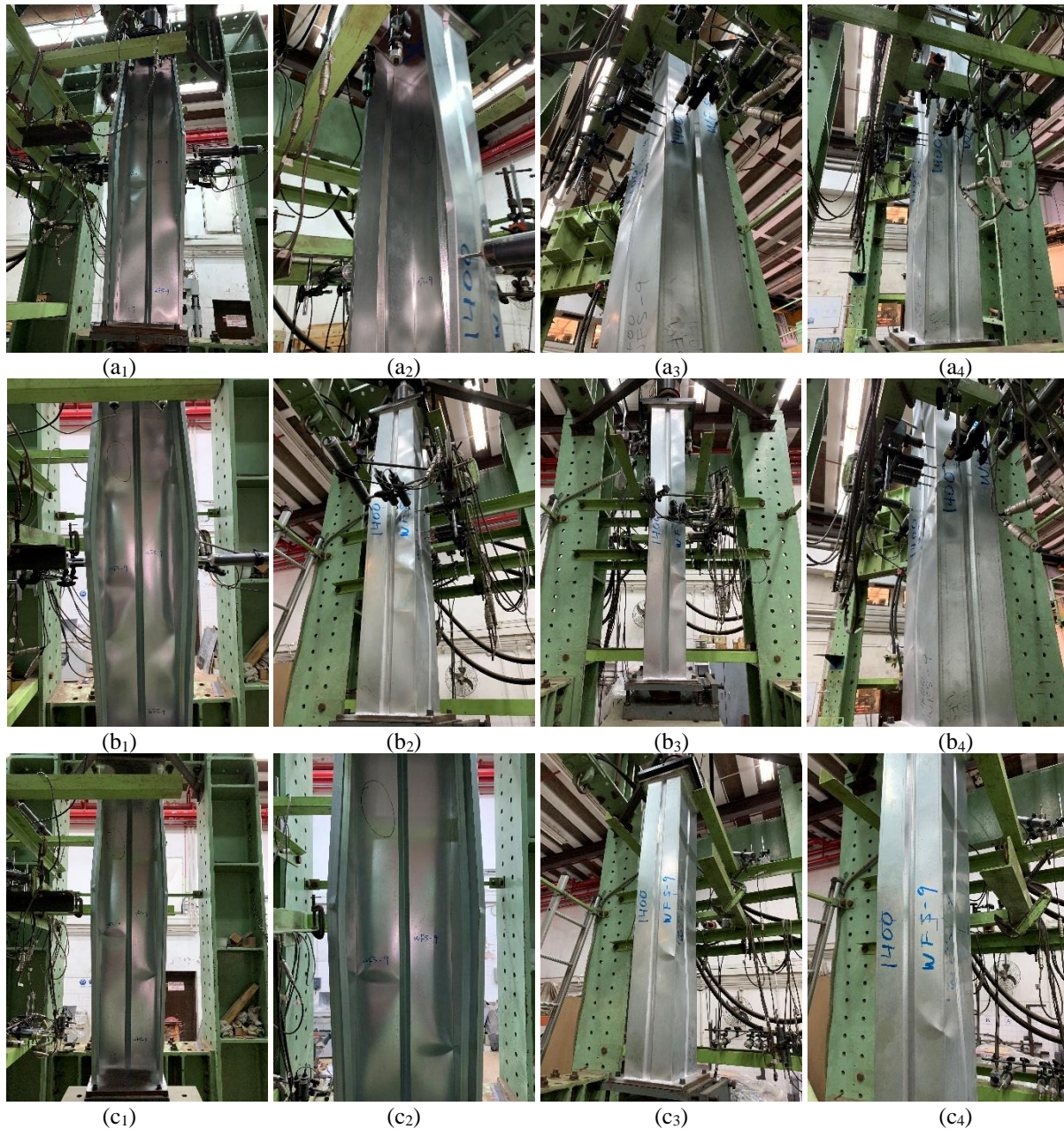
Figure 12: WFSLC-9 column deformed configurations (a) prior to collapse (equilibrium path ascending branch), (b) at the onset of collapse (failure mode) and (c) after the collapse (equilibrium path descending branch) or after the applied load has been removed.

The location of each plastic hinge is clearly illustrated further ahead in the paper – see Figs. 18+19.

(iv) The column axial shortening grows almost linearly with the applied load in the early loading stages only – as loading progresses, this growth becomes gradually more non-linear (see Figs. 14(a_1)-(a_4)).

(v) Confirming recent numerical findings (Martins *et al*. 2018), the distortional deformations play a dominant role in the behaviour of all the columns tested, when compared with their local and global counterparts. This fact is clearly illustrated and quantified in Figs. 14(b_1)-(b_4), providing the displacements measured by transducer T1 (those measured by transducer T11 are very similar and, thus, not shown here) – note that small portions of these displacements may be due to torsion present in the initial imperfections.

Figure 13: WSLC-1 column deformed configurations (a) prior to collapse (equilibrium path ascending branch) and (b) at the onset of collapse (failure mode).

(vi) The displacements measured by transducer T4 consist overwhelmingly of contributions from minor-axis flexure arising from the stress redistribution caused mostly by the distortional deformations but also, to a lesser extent, by the local ones (Martins *et al*. 2018). Rigorously speaking, these displacements may also contain tiny contributions from local and distortional deformations – recall that T4 is not placed exactly at the web-flange corner. It is interesting to note that this displacement points towards either the web (WSLC columns), as in plain lipped channels (Martins *et al*. 2018), or the lips (WFSLC columns). Moreover, a substantial increase is observed when the applied load reaches the critical buckling load level (see Fig. 14(c)). For applied loads below this level, the minor-axis flexural displacements are very small and stem exclusively from the initial geometrical imperfections.

(vii) As already mentioned in item (ii), the contribution from local deformations cannot generally be quantified in members affected by L-D interaction, regardless of the measurement location, because they always appear jointly with highly dominant distortional deformations. Indeed, the displacement measured by transducer T5 combines contributions from distortional, local and minor-axis flexural deformations (and possibly also a tiny contribution from the torsion present in the initially imperfect geometry). Only a rigorous modal analysis is able to quantify the above contributions (*e.g.*, (Martins *et al*. 2018)). Nonetheless, Figs. 10-13 provide fairly clear evidence of the presence of local deformations, particularly in the flanges of WSLC columns or in the web of WFSLC columns.

(viii) Since the WS-1 column exhibits two distortional half-waves, unlike the remaining specimens, its equilibrium paths (Figs. 14(a_4)-(d_4)) and deformed configurations (Figs. 13(a_1)-(b_4)) are quite distinct.
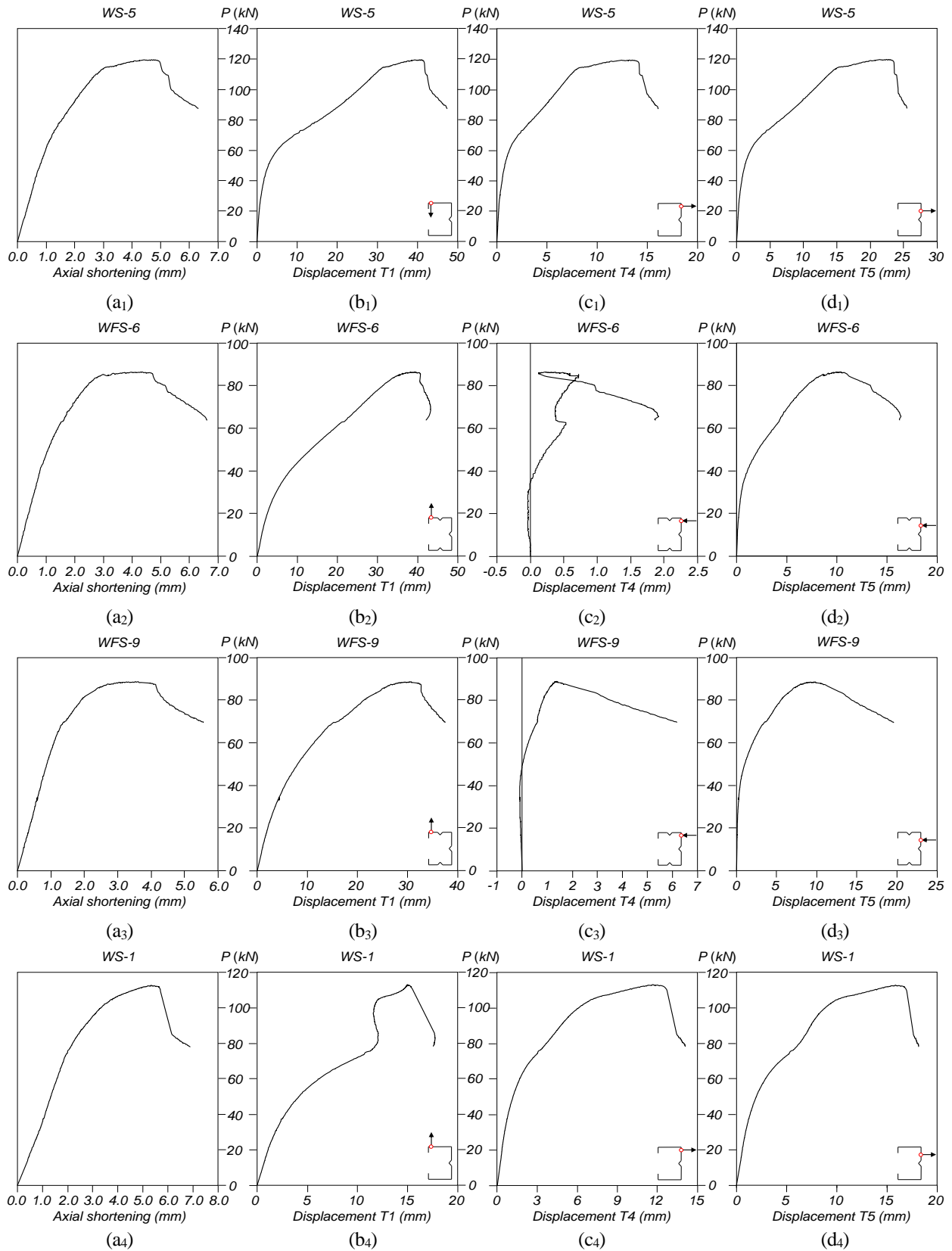
17

Figure 14: Experimental equilibrium paths: applied load *P* vs. (a) axial shortening, and displacements (b) T1, (c) T4 and (d) T5, for specimens (₁) WS-5, (₂) WFS-6, (₃) WFS-9 and (₄) WS-1.

18

First of all, the presence of initial geometrical imperfections with a large amplitude (see Table 4) leads to a highly non-linear behaviour since the early loading stages and until the applied load reaches approximately 80kN (close to the critical buckling load level). Between 80kN and 100kN, the displacement T1 remains practically constant, which is due to a fairly abrupt "configuration switch" from one to two distortional half-waves: the bottom and top "half columns" exhibit "inward" and "outward" flange-lip motions, respectively – this configuration is depicted in Fig. 13(a_1). Once more, again due to the initial geometrical imperfection shape, the deformed configuration is not symmetric, as attested by the fact that the mid-height cross-section exhibits "outward" flange-lip motions. As was mentioned in item (vi), the minor-axis flexural displacements point towards the web (see Fig. 14(c_4)). Lastly, Figs. 13(a_1)-(a_3) show that almost exclusively distortional deformations develop before the peak load is reached, since the local deformations only emerged at fairly high loads – for instance, visible flange local deformations can only be observed in Fig. 13(a_4), which concerns an applied load level well above those associated with Figs. 13(a_1)-(a_3)) – moreover, compare the flange deformed configuration shown in Fig. 13(a_4) with those appearing in Figs. 13(a_2)+(a_3). This behavioural feature is in agreement with the theory, since distortional buckling precedes local buckling load for this particular column ($R_{DL}\cong0.80$). Finally, note that L-D interaction occurs because the column is locally and distortionally rather slender – for less slender columns, the failure mode may be pure distortional (*i.e.*, not exhibit local deformations). Rigorously speaking, this column geometry is associated with the transition between "secondary local-bifurcation L-D interaction" and "true L-D interaction".

3.5.1.2 Secondary distortional-bifurcation L-D interaction
The results presented in this sub-section, which are qualitatively similar to those presented previously, concern columns WS-12 and WS-13 and consist of (i) photos showing column deformed configurations prior to collapse (Figs. 15(a_1)-(a_4) and Figs. 16(a_1)-(a_4)) or at the onset of collapse (Figs. 15(b_1)-(b_4) and Figs. 16(b_1)-(b_4)), and (ii) the recorded column axial shortening and displacements measured by transducers T1, T4 and T5 (Fig. 17). The observation of these results prompts the following comments:

(i) The equilibrium paths P vs. T5 (Fig. 17(d)), qualitatively similar to those obtained numerically (*e.g.*, Martins *et al*. 2018), are almost linear behaviour at the early loading stages, up until the vicinity of the critical (local) buckling load ($\cong$26kN – see Table 6). Thereafter, they become non-linear and associated with considerable post-critical strengths up until $P\cong$50kN (*i.e.*, close to the level of the theoretical critical distortional buckling load. For higher applied loads, there is noticeable strength erosion that happens while the distortional deformations grow fast and continues until the collapse – note that the failure load is much higher than the theoretical P_{crD} value (slender column). The emergence of pronounced distortional deformations (see, for instance, Fig. 17(b)) in columns where local buckling precedes distortional buckling characterises the "secondary distortional-bifurcation L-D interaction".

(ii) The photos displayed in Figs. 15 and 16, concerning deformed configurations either before or at the onset of collapse, show once again clear distortional (mostly) and local deformations even when local buckling precedes distortional buckling by a significant amount ($R_{DL}\cong$2.00) – this characterises L-D interaction (*e.g.*, Martins *et al*. 2018). On the other hand, it was observed that, for applied loads between the theoretical critical local and distortional buckling loads, mostly local deformations occur in these two columns – they are much more pronounced than those appearing in the columns addressed in the previous sub-section (unfortunately, there exist no photos backing/illustrating this assertion). Once distortional buckling is triggered, the distortional deformations grow rapidly and outweigh their local (and minor-axis flexural) counterparts.
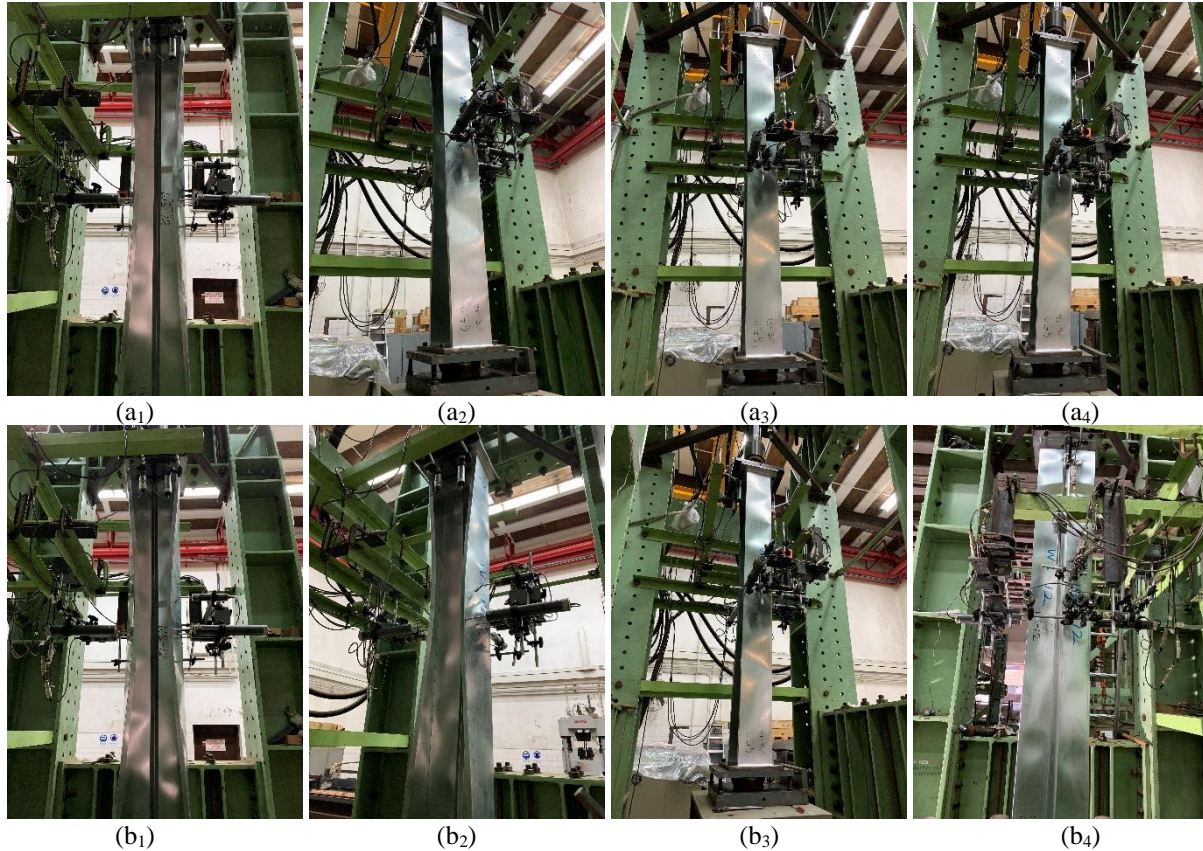
Figure 15: WSLC-12 column deformed configurations (a) prior to collapse (equilibrium path ascending branch) and (b) at the onset of collapse (failure mode).

(iii) The WS-12 and WS-13 column failure modes exhibit, once again, a single distortional half-wave that is akin to the critical distortional buckling mode and involves "inward" flange-lip motions (like all WSLC columns affected by "true L-D interaction").

(iv) The equilibrium paths P vs. T4 (Fig. 17(c)) show that significant minor-axis flexural displacements emerge, mainly after the development of considerable distortional deformations – they pointing towards the web, like in all the WSLC columns addressed in the previous sub-section.

(v) Unlike in most of the WSLC columns addressed in the previous sub-section, the plastic hinges now developed in the mid-height region (see, for instance, Figs. 16(b$_1$)-(b$_2$) and also Fig. 19), which is in close agreement with available numerical simulations (*e.g.*, Martins *et al*. 2016). These plastic hinge locations are very similar to those exhibited by the failure modes of columns buckling and failing in pure distortional modes (involving one half-wave) – this fact is responsible for the drastic strength erosion associated with this type of L-D interaction. Indeed, if the occurrence of L-D interaction could be fully prevented, the columns would collapse in pure local modes, which have a completely different nature – *i.e.*, L-D interaction causes a clear change in failure mode nature.

3.5.2 Failure loads

The values of the experimental failure loads (P_{Exp}) obtained in this investigation for the 31 WFSLC and WSLC column tested are given in Table 5. This table also shows (i) the maximum displacements at or just before the peak load, namely the axial shortening (Δ) and the flange-lip vertical displacement (Δ_D), and (ii) the observed failure mode nature ("L" and "D" stand for local and distortional deformation,

Figure 16: WSLC-13 column deformed configurations (a) prior to collapse (ascending branch) and (b) at the onset of collapse (failure mode).
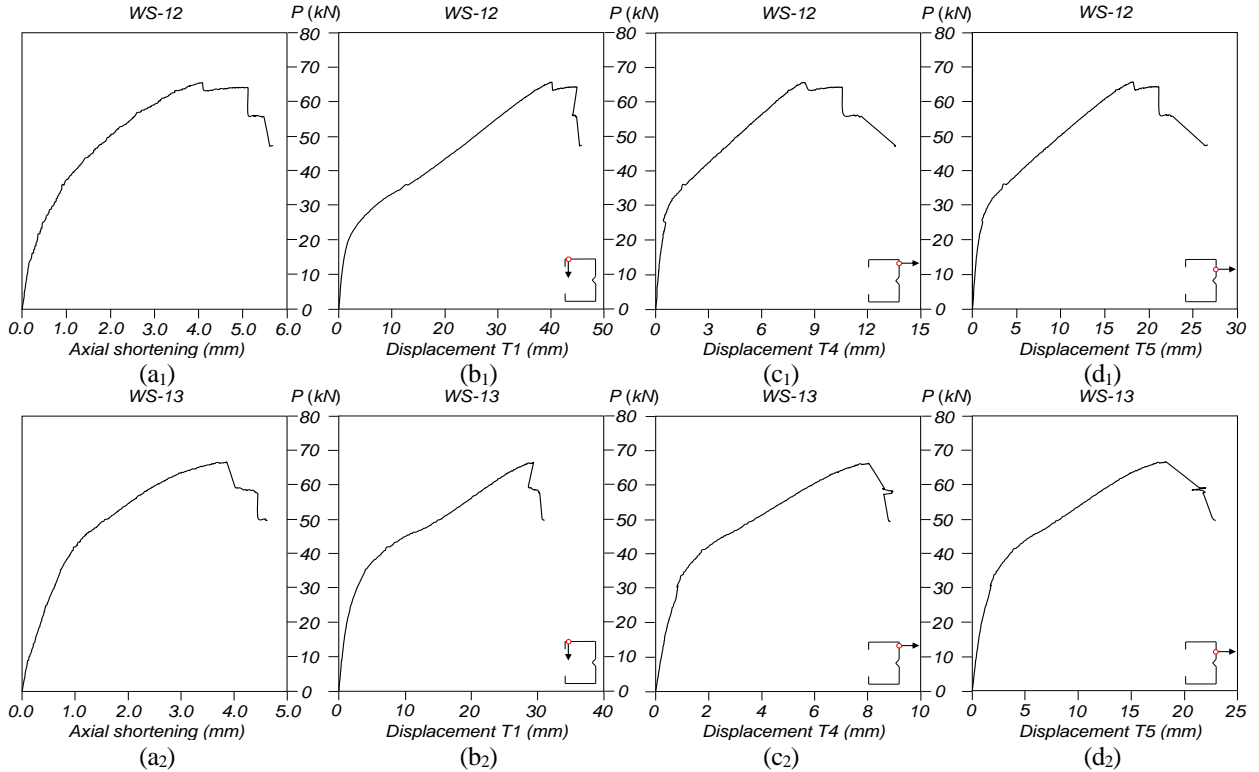

Figure 17: Experimental equilibrium paths: applied load P vs. (a) axial shortening, and displacements (b) T1, (c) T4 and (d) T5, concerning specimens (1) WS-12 and (2) WS-13.

respectively). As mentioned earlier, all specimens failed in L-D interactive modes and, with one single exception, exhibited one distortional half-wave – the exception was specimen WS-1, which exhibited two distortional half-waves. Out of the 30 specimens exhibiting one distortional half-wave, those exhibiting failure modes involving "inward" or "outward" flange-lip motions are identified in Table 5 by the designations "L-D⁻" and "L-D⁺", respectively – the numbers of distortional half-waves are given between brackets. The failure loads of the repeated specimens (WFS-5R, WFS-6R, WFS-9R, WS-5R and WS-6R) differed only by 1.5, 1.0, 1.3, 0.2 and 1.8% from their "original" counterparts, thus indicating an excellent reliability of the test set-up and procedure. In addition, the "original" and repeated specimens showed similar deformed configurations at the onset of collapse – the small failure load differences are naturally attributed to the distinct initial geometrical imperfections. Finally, Figs. 18 and 19 show photos of the whole sets of WFSLC and WSLC specimens after the completion of the experimental procedure, showing their deformed configurations once the applied load has been fully removed.

Table 5: Column experimental failure loads, corresponding displacements and observed failure mode natures.

Specimen	P_{Exp} (kN)	$\varDelta$ (mm)	$\varDelta_D$ (mm)	Failure mode nature
WFS-1	86.1	4.6	44.5	L+D(1)⁺
WFS-2	86.5	4.1	44.7	L+D(1)⁺
WFS-3	85.9	4.1	40.5	L+D(1)⁺
WFS-4	115.8	4.3	39.1	L+D(1)⁺
WFS-5	110.9	4.7	45.1	L+D(1)⁺
WFS-5R	112.6	5.1	44.0	L+D(1)⁺
WFS-6	86.5	4.4	39.5	L+D(1)⁺
WFS-6R	85.6	3.8	39.1	L+D(1)⁺
WFS-7	71.2	4.3	-46.8	L+D(1)⁻
WFS-8	86.5	4.0	39.4	L+D(1)⁺
WFS-9	88.7	3.5	30.8	L+D(1)⁺
WFS-9R	89.9	3.9	32.3	L+D(1)⁺
WFS-10	86.4	3.5	35.0	L+D(1)⁺
WFS-11	87.7	3.8	36.0	L+D(1)⁺
WFS-12	80.9	3.9	-44.1	L+D(1)⁻
WFS-13	84.3	4.1	38.7	L+D(1)⁺
WS-1	112.7	5.3	-15.0	L+D(2)
WS-2	117.9	6.4	-9.8	L+D(1)⁻
WS-3	120.7	4.2	-17.3	L+D(1)⁻
WS-4	122.4	3.5	-24.2	L+D(1)⁻
WS-5	119.6	4.8	-40.9	L+D(1)⁻
WS-5R	119.8	4.9	-25.3	L+D(1)⁻
WS-6	120.5	4.4	-30.4	L+D(1)⁻
WS-6R	118.4	4.2	-37.7	L+D(1)⁻
WS-7	120.3	3.6	-30.1	L+D(1)⁻
WS-8	118.1	5.0	-33.5	L+D(1)⁻
WS-9	86.7	5.4	-44.7	L+D(1)⁻
WS-10	86.0	5.6	-44.3	L+D(1)⁻
WS-11	68.9	5.2	-46.9	L+D(1)⁻
WS-12	65.6	4.0	-40.0	L+D(1)⁻
WS-13	66.7	3.9	-29.4	L+D(1)⁻

Figure 18: Deformed configurations of all WFSLC specimens after the full removal of the applied load.

Figure 19: Deformed configurations of all WSLC specimens after the full removal of the applied load.

4. Direct Strength Method (DSM) design

This section presents the failure load estimates provided by the currently codified DSM-based column design curves, namely the local and distortional design curves, for the tested specimens, and compares them with the experimental failure loads obtained during this investigation. Since all specimens failed in L-D interactive modes, it makes no sense to compare their failure loads with the predictions of the global or local-global interactive design curves. Table 6 presents the (i) critical local and distortional buckling loads, obtained with GBTUL (Bebiano *et al.* 2018) on the basis of the measured geometries (Table 2) and determined elastic properties (Table 3), and (ii) local and distortional slenderness values, both required to obtain the DSM failure load predictions associated with distortional (P_{nD}) and local (P_{nL}) collapses. In addition, Figs. 20(a)-(b) show the P_{Exp}/P_{nD} vs. λ_D and P_{Exp}/P_{nL} vs. λ_L plots concerning all the experimental failure loads obtained in this work. The observation of these results leads to the following comments:

(i) The comparison between the values given in Tables 1 and 6 shows that the critical buckling load ratios (R_{DL}) of the planned and tested specimens differ mainly in the critical distortional buckling loads — the latter are a bit lower, particularly for the WFSLC columns. This is due to a combination of less wide lips (compared to the designed ones) and less efficient web-stiffeners, since their horizontal (parallel to the flanges) depth is, in most cases, lower than 15mm (the designed value).

(ii) Fig. 20 shows clearly that the currently codified local and distortional DSM design curves are unable to provide acceptable failure load predictions for columns undergoing L-D interaction, since they do not capture the associated failure load erosion — all column failure loads are overestimated and the overestimation is more pronounced for the slender columns. Moreover, the DSM distortional design curve naturally outperforms its local counterpart, as attested by comparing their statistical indications given in Fig. 20(a)+(b) — recall that it predicts lower failure loads (for $\lambda_L=\lambda_D$). This confirms previous findings (*e.g.*, Martins *et al.* 2017a) and demonstrates, once more, that it is absolutely indispensable to equip the CFS technical/scientific community with efficient (safe, accurate and reliable) DSM-based design rules that are able to capture adequately the failure load erosion stemming from L-D interaction.

Table 6: Tested column specimens (i) geometries, (ii) failure loads, (iii) critical (local and distortional) buckling loads and (iv) local and distortional slenderness values.

| Specimen	D	B	b_l	t^*	L	f_y	P_y	P_{Exp}	P_{crL}	P_{crD}	R_{DL}	λ_L	λ_D
	(mm)	(mm)	(mm)	(mm)	(mm)	(MPa)	(kN)	(kN)	(kN)	(kN)	(-)	(-)	(-)
WS-1	279.6	150.5	15.7	1.513	2501	530	514.0	112.7	89.7	72.8(2)	**0.81**	2.39	2.66
WS-2	278.7	151.1	16.1	1.515	2201	530	515.8	117.9	90.0	81.9(1)	**0.91**	2.39	2.51
WS-3	220.6	129.8	15.5	1.513	1701	530	427.8	120.7	103.0	94.4(1)	**0.92**	2.04	2.13
WS-4	222.3	129.6	16.0	1.522	1502	530	435.3	122.4	106.3	107.3(1)	**1.01**	2.02	2.01
WS-5	261.9	150.3	16.4	1.512	1803	530	499.0	119.6	88.4	86.7(1)	**0.98**	2.38	2.40
WS-5R	262.7	149.9	16.3	1.520	1801	530	501.4	119.8	90.2	87.6(1)	**0.97**	2.36	2.39
WS-6	258.8	150.6	16.3	1.513	1552	530	496.9	120.5	88.0	94.0(1)	**1.07**	2.38	2.30
WS-6R	259.5	149.8	15.6	1.508	1554	530	491.5	118.4	87.1	85.8(1)	**0.98**	2.38	2.39
WS-7	269.1	160.3	16.0	1.501	1500	530	516.6	120.3	79.3	88.1(1)	**1.11**	2.55	2.42
WS-8	269.0	160.4	15.7	1.511	1651	530	520.4	118.1	80.7	82.1(1)	**1.02**	2.54	2.52
WS-9	274.5	170.4	16.7	1.215	1653	560	463.1	86.7	39.3	59.1(1)	**1.50**	3.43	2.80
WS-10	272.7	171.6	16.4	1.219	1955	560	465.0	86.0	39.1	50.7(1)	**1.29**	3.45	3.03
WS-11	252.1	151.2	16.5	1.013	1753	600	380.4	68.9	26.7	45.4(1)	**1.70**	3.78	2.90
WS-12	253.3	151.6	16.3	1.011	1652	600	379.5	65.6	26.3	45.6(1)	**1.73**	3.80	2.88
WS-13	255.5	150.9	15.8	1.012	1350	600	378.3	66.7	26.5	49.9(1)	**1.88**	3.78	2.75
WFS-1	252.4	202.2	15.9	0.991	1752	600	453.5	86.1	62.9	47.5(1)	**0.76**	2.69	3.09
WFS-2	252.5	201.5	15.8	1.003	1652	600	462.3	86.5	65.0	55.8(1)	**0.86**	2.67	2.88
WFS-3	252.2	201.6	15.9	1.002	1503	600	457.4	85.9	65.6	60.4(1)	**0.92**	2.64	2.75
WFS-4	250.1	220.5	15.8	1.209	1254	560	533.1	115.8	118.7	106.0(1)	**0.89**	2.12	2.24
WFS-5	271.4	241.2	15.0	1.218	1299	560	571.6	110.9	110.2	82.8(1)	**0.75**	2.28	2.63
WFS-5R	273.8	240.2	15.0	1.220	1299	560	574.9	112.6	108.6	85.8(1)	**0.79**	2.30	2.59
WFS-6	270.6	182.6	16.2	1.006	1702	600	443.1	86.5	55.7	49.2(1)	**0.88**	2.82	3.00
WFS-6R	273.3	181.4	15.8	1.009	1703	600	450.5	85.6	55.3	54.3(1)	**0.98**	2.85	2.88
WFS-7	283.8	193.2	17.2	0.994	2005	600	458.5	71.2	50.9	40.3(1)	**0.79**	3.00	3.37
WFS-8	252.5	222.0	15.5	0.998	1355	600	479.8	86.5	65.6	63.7(1)	**0.97**	2.70	2.74
WFS-9	273.0	182.7	17.7	0.994	1398	600	443.3	88.7	53.2	70.9(1)	**1.33**	2.89	2.50
WFS-9R	271.5	182.1	16.4	1.010	1401	600	452.2	89.9	56.0	76.2(1)	**1.36**	2.84	2.44
WFS-10	270.8	182.6	15.6	0.998	1504	600	446.1	86.4	55.5	64.1(1)	**1.16**	2.84	2.64
WFS-11	282.6	191.6	17.5	1.000	1501	600	464.9	87.7	53.0	68.6(1)	**1.29**	2.96	2.60
WFS-12	300.5	202.0	16.9	0.999	1654	600	490.9	80.9	48.0	60.0(1)	**1.25**	3.20	2.86
WFS-13	302.6	201.6	16.7	1.008	1502	600	489.6	84.3	48.4	58.4(1)	**1.22**	3.19	2.90
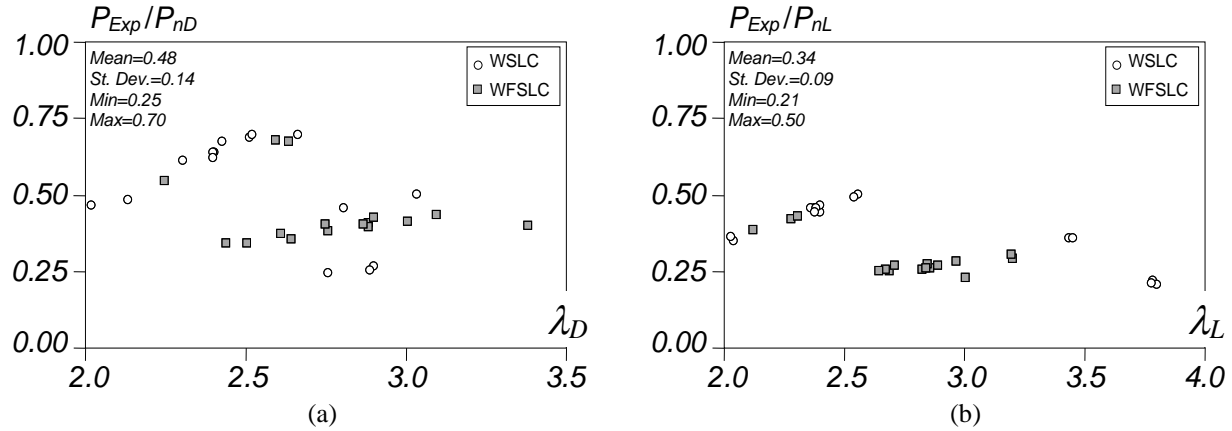
Figure 20: Plots of (a) P_{Exp}/P_{nD} vs. λ_D and (b) P_{Exp}/P_{nL} vs. λ_L of all WSLC and WFSLC specimens tested.

In view of what was mentioned in item (ii) above, the authors are currently working on the development and validation of a DSM-based design approach for CFS columns affected by L-D interaction that (i) predicts safely, accurately and reliably the whole set of available experimental and numerical failure loads, and (ii) hopefully will be a strong candidate for codification in the near future. The work under way, which will be reported soon, (i) includes the performance of fresh numerical simulations, prompted by the experimental results reported in this work and using a shell finite element model validated against them, and (ii) takes into account the currently available (preliminary) DSM-based design proposals (Silvestre *et al*. 2012, Martins *et al*. 2017a, Matsubara *et al*. 2019).

4. Conclusions

This work reported an experimental investigation, planned at the University of Lisbon and carried out at The University of Hong Kong, dealing with the structural behaviour and ultimate strength of cold-formed steel web-stiffened (WSLC) and web-flange-stiffened lipped channel (WFSLC) columns undergoing several levels of local-distortional (L-D) interaction. After addressing the selection of the column specimen geometries, which ensured different critical distortional-to-local buckling load ratios, the paper described (i) the mechanical material properties of the specimens tested, obtained through tensile coupon tests, and (ii) the test set-up and the procedures related to the test performance, including the location of the displacement measurements and the initial geometrical imperfections recorded. Then, attention was turned to the presentation and discussion of the results obtained from the 31 column tests, namely (i) non-linear load-displacement equilibrium paths, (ii) photos showing deformed configurations along those paths (including the failure modes) and (iii) failure loads. Lastly, the paper compared the experimental failure loads obtained in this investigation with their estimates provided by the currently codified DSM (Direct Strength Method) local and distortional design curves.

This investigation provided clear experimental evidence about the occurrence of L-D interaction in WSLC and WFSLC slender columns for a fairly large range of critical distortional-to-local buckling load ratios, comprised between 0.75 and 1.88. In addition, it (i) enabled the acquisition of substantial experimental failure load data (the main purpose of this investigation) and (ii) provided experimental validation/confirmation of several findings obtained in the recent past, on the basis of numerical results (similar load-displacement equilibrium paths and failure modes) and (iii) showed that L-D interaction is mostly governed by distortional deformations (even when local buckling precedes its distortional counterpart). The comparison between the experimental failure loads and their predictions provided by the currently codified local and distortional DSM design curves confirmed the high impact

25

of L-D interaction, in the sense that it leads to substantial failure load erosion, and also the inability of the above design curves in capturing this impact. It also demonstrated, once more, the need for design rules able to handle properly column L-D interactive failures. The authors are currently working on fulfilling this need, by developing an efficient DSM-based design approach intended for cold-formed steel columns affected by L-D interaction that can be proposed for codification – the fruits bore by this research effort will be reported soon. In this context, the column failure loads acquired in this work, together with those already available (either experimental or numerical), will certainly play a pivotal role in paving the way towards the sought codification – the ultimate goal of this ongoing investigation.

Acknowledgments

References

ASTM-E8M (2016). "Standard test methods for tension testing of metallic materials", ASTM E8M-16, West Conshohocken, PA, USA.

Bebiano, R., Camotim, D., Gonçalves, R. (2018). "GBTUL 2.0 – a second-generation code for the GBT-based buckling and vibration analysis of thin-walled members", *Thin-Walled Structures*, 124(March), 235-257.

Camotim, D., Dinis, P.B., Martins, A.D. (2016). "Direct Strength Method (DSM) – a general approach for the design of cold-formed Steel structures", *Recent Trends in Cold-Formed Steel Construction*, C. Yu (ed.), Woodhead Publishing (Series in Civil and Structural Engineering), Amsterdam, 69-105.

Camotim, D., Dinis, P.B., Martins, A.D., Young, B. (2018). "Review: Interactive behaviour, failure and DSM design of cold-formed steel members prone to distortional buckling", *Thin-Walled Structures*, 128(July), 12-42.

Chen, J., Chen, M.-T., Young, B. (2019). "Compression tests of cold-formed steel C- and Z-sections with different stiffeners", *Journal of Structural Engineering* (ASCE), 145(5), 04019022 (10 pages).

Dinis, P.B., Young, B., Camotim, D. (2014). "Local-distortional interaction in cold-formed steel rack-section columns", *Thin-Walled Structures*, 81(August), 185-194.

Dinis, P.B., Camotim, D. (2015). "Cold-formed steel columns undergoing local-distortional coupling: behaviour and direct strength prediction against interactive failure", *Computers & Structures*, 147(January), 181-208.

He, Z., Zhou, X., Liu, Z., Chen, M. (2014). "Post-buckling behaviour and DSM design of web-stiffened lipped channel columns with distortional and local mode interaction", *Thin-Walled Structures*, 84(November), 189-203.

Huang, Y., Young, B. (2014). "The art of coupon tests", *Journal of Constructional Steel Research*, 96(May), 159-175.

Kwon, Y.B., Hancock, G.J. (1992). "Tests of cold-formed channels with local and distortional buckling", *Journal of Structural Engineering* (ASCE), 118(7), 1786-1803.

Kwon, Y.B., Kim, B.S., Hancock, G.J. (2009). "Compression tests of high strength cold-formed steel channel with buckling interaction", *Journal of Constructional Steel Research*, 65(2), 278-289.

Kwon, Y.B., Kim, N.K., Kim, B.S. (2005). "A study on the direct strength method for compression members undergoing mixed mode buckling", *Proceedings of 3rd International Symposium on Steel Structures* (ISSS'05 – Seoul 10-11/03), 108-119.

Loughlan, J., Yidris, N., Jones, K. (2012). "The failure of thin-walled lipped channel compression members due to coupled local-distortional interactions and material yielding", *Thin-Walled Structures*, 61(December), 14-21.

Martins, A.D., Dinis, P.B., Camotim, D., Providência P. (2015). "On the relevance of local-distortional interaction effects in the behaviour and design of cold-formed steel columns", *Computers & Structures*, 160(November), 57-89.

Martins, A.D., Dinis, P.B., Camotim, D. (2016). "On the influence of local-distortional interaction in the behaviour and design of cold-formed steel web-stiffened lipped channel columns", *Thin-Walled Structures*, 101(April), 181-204.

Martins, A.D., Camotim, D., Dinis, P.B. (2017a). "On the direct strength design of cold-formed steel columns failing in local-distortional interactive modes", *Thin-Walled Structures*, 120(November), 432-445.

Martins, A.D., Camotim, D., Dinis, P.B. (2017b). "Behaviour and DSM design of stiffened lipped channel columns undergoing local-distortional interaction", *Journal of Constructional Steel Research*, 128(January), 99-118.

Martins, A.D., Camotim, D., Gonçalves, R., Dinis P.B. (2018). "On the mechanics of local-distortional interaction in thin-walled lipped channel columns", *Thin-Walled Structures*, 125(April), 187-202.

Matsubara, G.Y., Batista, E.M., Salles, G.C. (2019). "Lipped channel cold-formed steel columns under local-distortional buckling mode interaction", *Thin-Walled Structures*, 137(April), 251-270.

Schafer, B.W. (2008). "Review: the direct strength method of cold-formed steel member design", *Journal of Constructional Steel Research*, 64(7-8), 766-778.

Schafer, B.W. (2019). "Advances in the Direct Strength Method of cold-formed steel design", *Thin-Walled Structures*, 140(July), 533-541.

Silvestre, N., Camotim, D., Dinis, P.B. (2012). "Post-buckling behaviour and direct strength design of lipped channel columns experiencing local/distortional interaction", *Journal of Constructional Steel Research*, 73(June), 12-30.

Yang, D., Hancock, G.J. (2004). "Compression tests of high strength steel channel columns with interaction between local and distortional buckling", *Journal of Structural Engineering* (ASCE), 130(12), 1954-1963.

Yap, D.C.Y., Hancock, G.J. (2008). "Experimental study of complex high-strength cold-formed cross-shaped steel section", *Journal of Structural Engineering* (ASCE), 134(8), 1322-1333.

Yap, D.C.Y., Hancock, G.J. (2011). "Experimental study of high strength cold-formed stiffened-web C-sections in compression", *Journal of Structural Engineering* (ASCE), 137(2), 162-172.

Young, B., Rasmussen, K.J.R. (1998). "Design of lipped channel columns", *Journal of Structural Engineering* (ASCE), 124(2), 140-148.

Young, B., Rasmussen, K.J.R. (1999). "Shift of effective centroid in channel columns", *Journal of Structural Engineering* (ASCE), 125(5), 524-531.

Young, B., Silvestre, N., Camotim, D. (2013). "Cold-formed steel lipped channel columns influenced by local-distortional interaction: strength and DSM design", *Journal of Structural Engineering* (ASCE), 139(6), 1059-1074.